

## A Two-Box Model of a Zonal Atmospheric Circulation in the Tropics

MICHAEL A. KELLY\* AND DAVID A. RANDALL

*Department of Atmospheric Science, Colorado State University, Fort Collins, Colorado*

(Manuscript received 8 September 1999, in final form 12 February 2001)

### ABSTRACT

A simple fixed-SST model of a zonal circulation in the tropical atmosphere has been developed that has separate boxes for the ascending and descending branches of the atmospheric circulation. This circulation resembles the Walker circulation. This is the first box model to determine the fractional widths of the warm and cold pools. The atmospheric model contains an explicit hydrologic cycle, a simplified but physically based radiative transfer parameterization, and interactive clouds.

Results indicate that the intensity of the tropical circulation is crucially dependent on the amount and vertical distribution of water vapor above the cold-pool boundary layer (CPBL). In response to increasing precipitable water over the CPBL, the radiative cooling rate of the free troposphere increases. To a good approximation, subsidence warming balances radiative cooling in the subsiding branches of the circulation. If the fractional width of the cold pool (CP) does not change too much, the circulation must intensify as the subsidence rate increases. To compensate for a stronger circulation and to restore energy balance in the Walker cell, the precipitable water over the warm pool (WP) must decrease. A "moist-outflow" experiment shows that the Walker circulation intensifies if air is advected to the subsiding regions from lower altitudes in the WP. As the advection level decreases, air supplied to the CP becomes warmer and moister, and so the column water vapor in the CP free troposphere increases. The mechanism described above then leads to a strengthening of the circulation. This moist-outflow experiment also shows that when the authors try to moisten the atmosphere by specifying a lower advection level for water vapor, the atmosphere adjusts so as to dry out. This effect is very strong.

### 1. Introduction

The steady tropical ocean–atmosphere general circulation remains inadequately understood. Many previous studies have discussed sensitivities of the tropical climate (Lindzen and Nigam 1987; Ramanathan and Collins 1991), or have described the linear response of the tropical climate to small perturbations (Gill 1980; Geisler 1981; Rosenlof et al. 1986). The value of these studies was primarily to show the processes and interactions that must be considered in a theory of the steady tropical climate. Recent studies with box models (Pierrehumbert 1995; Sun and Liu 1996; Miller 1997; Larson et al. 1999, hereinafter LHK; Sherwood 1999; Clement and Seager 1999) have improved our understanding because they capture essential processes of the tropical ocean–atmosphere circulation in a simplified way. The applicability of these box models is somewhat limited, however, because of their extreme simplifications. For example, Pierrehumbert (1995), hereinafter referred to as P95, neglected cloud-radiative effects and specified the potential temperature difference between the upper

and lower branches of the tropical circulation. The atmospheric momentum budget was ignored in P95, Miller (1997; hereinafter M97), and LHK. Sherwood (1999) incorporated a simple momentum budget but specified the vertical structure of the atmosphere.

A recent paper by Kelly et al. (1999; hereinafter KRS) presented and discussed results from a simple model of the tropical warm pool (WP). They showed that clear-sky radiative–convective equilibria of the WP ocean–atmosphere system do not occur. As the sea surface temperature (SST) increases, the precipitable water over the WP ( $W_w$ ) tends to increase, and so the longwave trapping effect of water vapor reduces the outgoing longwave radiation (OLR) and leads to a runaway greenhouse (Ingersoll 1969). When cloud radiative effects are included, the absorbed shortwave radiation is reduced and a very warm, very dry equilibrium is possible, but it does not resemble the observations. This high-SST, low- $W$  combination results in a relatively large value of the OLR that can balance the absorbed solar radiation. KRS also showed that realistic prescribed horizontal transports of energy and moisture make a realistic equilibrium possible. These results are consistent with P95 who showed that a low water vapor region that is efficient at radiating energy to space is needed in order for the Tropics to reach a stable equilibrium. Because the horizontal transports and wind speed were specified, however, results presented in KRS fall far short

\* Current affiliation: Logicon TASC, Inc., Chantilly, Virginia.

Corresponding author address: Dr. Michael A. Kelly, Logicon TASC, 4801 Stonecroft Blvd., Chantilly, VA 20151.  
E-mail: makelly@tasc.com

of a simulation of the tropical climate. In order to more satisfactorily simulate the climate, the lateral exchanges of atmospheric moisture, energy, and momentum must be computed.

The primary goal of this study is to add additional physics to the model of KRS in order to study the lateral energy and moisture exchanges between the WP and cold pool (CP). This requires the wind speed to be computed, rather than specified as in KRS. We invoke a simplified momentum balance for the atmosphere. As with any simple “toy” model, our motivation is to simulate the dominant interactions among the various physical processes in the atmosphere while neglecting secondary processes. This approach requires a priori assumptions as to which interactions are dominant. We explore the importance of some interactions by alternately including and excluding them in sensitivity experiments.

The present paper concentrates on modeling the atmospheric circulation in an idealized way. We have chosen to fix SSTs, which eliminates the very important atmosphere–ocean interactions. We have also chosen to fix the depth of the boundary layer. LHK demonstrated the sensitivity of climate simulations from a two-box model to fluctuations of the tropical boundary layer depth.

The widths of the WP and CP are calculated as those that balance the energy budget for the given tropical SST distribution. We assume that the model evolves to a stable, equilibrium configuration with no net heating/cooling in either box. If either box is subject to net heating/cooling, then the system is assumed to evolve until a stable solution is found. Because tropical dynamics require the temperature gradient in the tropical free troposphere to be small (Charney 1963), the energy flux divergence in either box must adjust so as to reduce the temperature gradient. We postulate that the system adjusts the size of the WP and CP in response to increased heating/cooling in order to maintain the energy balance and to keep the tropical temperature gradients small. Accordingly, we calculate the equilibrium widths for the WP and CP as those required to maintain the energy balance in the Tropics.

As described later, we use a simple time-marching scheme to find the equilibrium widths. Only the equilibrium solutions are physically meaningful, however, and so the reader is cautioned to avoid viewing model transitions as time-dependent behavior.

The response of the atmosphere to perturbations is an interesting problem in itself. Recent efforts have (appropriately) concentrated on the response of the coupled system, but the behavior of the atmosphere in the context of a box model has not been adequately addressed. Without understanding the atmosphere-only solution, it is often difficult to fully understand the coupled solution. What are the mechanisms for adjustment within the atmosphere? Our results give insight into the behavior of the atmosphere, precisely because the coupled response has been eliminated.

The paper is organized as follows. We give an overview of the model in section 2. In section 3, we derive a simplified momentum budget for the CP boundary layer (CPBL) and detail our calculation of the dry static energy difference between the upper and lower branches of the simulated Walker circulation. We also show how the widths of the CP and WP are calculated. Section 4 briefly describes the WP model. We present stand-alone results for the CP model in section 5. Section 6 shows how the WP and CP models are coupled. We present results from the complete model in section 7. Section 8 gives a summary and conclusions. Throughout this paper, we contrast and compare our model with those of P95, M97, and LHK.

## 2. A quick overview of the model

The idealized circulation consists of upper-tropospheric outflow from the WP to the CP and a lower-tropospheric inflow from the CP to the WP (Fig. 1). Based on data from the European Centre for Medium-Range Weather Forecasts (ECMWF) reanalysis, we assume that the zero-wind level occurs at 600 mb. The easterly mass flux over the CP is forced by a horizontal pressure gradient, which is induced by an SST gradient. The air exiting the CPBL is replaced by subsiding air. Over the WP, the westward horizontal mass flux decreases to zero at the western boundary, as the mass flow turns upward and departs the boundary layer in the convectively active region. As the convective outflow travels eastward over the CP, it undergoes radiative cooling and subsidence warming. A positive zonal pressure gradient decelerates the wind as it crosses the CP. We require that the eastward mass flux decrease to zero at the eastern boundary.

SST gradients across the tropical Pacific Ocean are observed to be very small, especially in the WP. We assume that the SST is uniform across the WP ( $T_{sw}$ ) and varies linearly from  $T_{sw}$  at the CP–WP boundary to  $T_{se}$  at the eastern boundary of the CP. The mean CP SST is therefore given by  $T_{sc} = 1/2(T_{sw} + T_{se})$ . Horizontal temperature gradients in the tropical free troposphere are small because of weak rotation (Charney 1963). Consistent with these findings, we assume that the free-tropospheric temperature is horizontally uniform for the WP region. In the CP upper troposphere, a negative zonal pressure gradient decelerates the westerly flow. Figure 2 shows the assumed temperature profiles in the two regions. Following P95, the free-tropospheric temperature profile is assumed to be identical in the CP and WP. We represent the trade wind inversion (TWI) of the CP region as a discontinuous jump in temperature.

## 3. CP model

### a. Basic structure

P95 referred to the subsiding branches of the tropical circulation as “radiator fins” because they efficiently

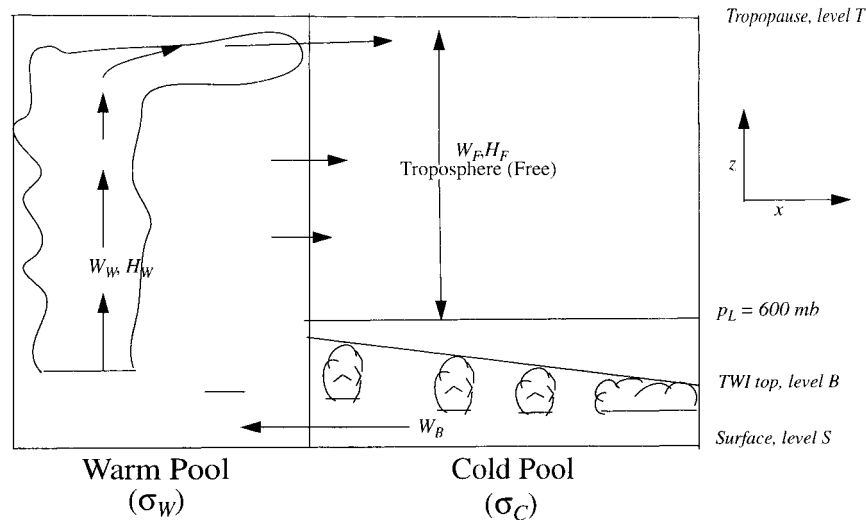


FIG. 1. Schematic of the two-box model. Here  $\sigma_c$  and  $\sigma_w$  are the widths of the CP and the WP; TWI is the trade wind inversion level,  $p_L$  is the pressure level separating the lower and upper troposphere and at which the zero-wind level is assumed to occur,  $W_w$  is the precipitable water over the WP,  $W_F$  is the vertically integrated water vapor in the free troposphere of the CP region,  $W_B$  is the vertically integrated water vapor in the CP boundary layer, and  $H_F$  and  $H_w$  are the vertically moist static energy in the free troposphere of the CP region and the WP regions, respectively.

radiate to space excess energy that is transported laterally to the CP region from the WP region. The widths of the CP ( $\sigma_c$ ) and the WP ( $\sigma_w$ ) adjust in our model so that the vertically integrated energy flux divergence in the CP balances the energy transported by the WP. The total width of the basin,  $\sigma = \sigma_w + \sigma_c$ , is specified to be  $1.5 \times 10^7$  m. We also make use of the fractional widths of the CP ( $a_c \equiv \sigma_c/\sigma$ ) and the WP ( $a_w \equiv \sigma_w/\sigma$ ). See Table 1 for a list of the variables of the model.

Vertical motion in the CP free troposphere follows from the balance between subsidence warming and radiative cooling. Based on ECMWF reanalysis data, the subsidence rate is assumed to increase linearly from zero at the tropopause to a maximum at 600 mb, and to be independent of height between 600 mb and the TWI. This allows us to simplify the continuity equations for the CP region. A simple water vapor advection model diagnoses the precipitable water in the free troposphere. A radiative transfer parameterization, similar to that used for the WP region, gives the radiative cooling rate in the free troposphere. As described earlier, we have chosen to fix SSTs for this study. Because stratocumulus clouds in the CP region act primarily as a thermostat for SSTs (Miller 1997), we neglect cloud radiative effects in the CP region.

Figure 3 illustrates the three-layer structure assumed for the CP region of the atmosphere. Westerlies and easterlies are confined to altitudes above and below the pressure level  $p_L$ . As previously stated, we assume that the zero-wind level occurs at 600 mb, and so  $p_L = 600$  mb. The pressure level,  $p_B$ , at the top of the boundary layer slopes from west to east. The symbols  $M_L$  and  $M_B$  rep-

resent mass fluxes through  $p_L$  and  $p_B$ , respectively. We define  $\Pi_B \equiv p_s - p_B$ ,  $\Pi_+ \equiv p_B - p_L$ , and  $\Pi_L \equiv \Pi_B + \Pi_+$ , where  $p_s$  is the surface pressure. The subscripts  $B$ ,  $+$ , and  $L$  denote quantities in the boundary layer, quantities in the layer between the boundary layer top and the zero-wind level, and mean quantities for the entire layer of easterlies, respectively. Thus,  $u_B$  refers to the zonal wind in the boundary layer,  $u_+$  represents the zonal wind in the layer between  $p_B$  and  $p_L$ , and  $u_L \equiv (u_+ \Pi_+ + u_B \Pi_B) \Pi_L^{-1}$  is the mass-weighted mean zonal wind in the layer of easterlies. The subscript  $U$  (for upper layer) refers to quantities in the layer of westerlies.

The governing equations for the CP model are given in Table 2. There are 5 equations for the 5 unknowns  $u_B$ ,  $\sigma_c$ ,  $q_L$ ,  $\omega_L$ , and  $M_L$ ;  $q_L$  is the water vapor specific humidity entering/leaving the WP in the lower atmosphere and  $\omega_L$  is the subsidence rate at 600 mb in the CP. Here  $U_A \equiv -u_L \Pi_L g^{-1}$  is the atmospheric mass flux circulating through the WP and CP with  $g$  being the acceleration of gravity;<sup>1</sup>  $s_U$  represents the mass-weighted vertical mean of dry static energy  $s$  between 600 mb and the tropopause;  $E_C$  is the mean surface evaporation rate in the CP;  $N_{\infty C}$  is the net downward energy flux at the tropopause of the CP;  $N_{SC}$  is the net downward energy flux at the CP surface;  $\omega_L$  is the vertical velocity at level  $p_L$ ; and  $\delta R_F$  is the net radiative cooling rate in the free troposphere. The symbol  $\Delta$  denotes the evaporation efficiency, which is defined as  $(E - P)/E$  and

<sup>1</sup> The units should be kilograms per second for a true mass flux, but the units of  $U_A$  are kilograms per meter per second. This difference occurs because our equations describe motions in the  $x$ - $z$  plane.

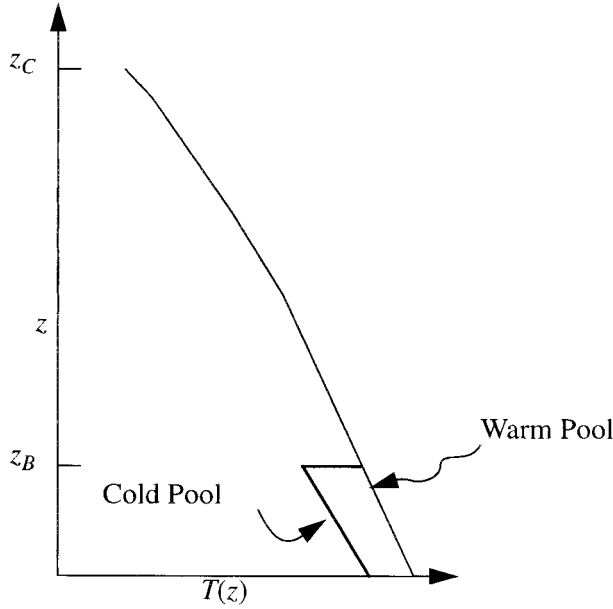


FIG. 2. Schematic illustrating the idealized vertical temperature profiles in the CP and WP [ $z_B$  and  $z_C$  are the heights of the boundary layer and the convective layer (tropopause)].

is discussed later. The symbols  $\xi_1$ ,  $\xi_2$ , and  $\xi_3$  were introduced for convenience in order to write the momentum equation concisely. These symbols are difficult to relate to the expected terms in a conventional set of momentum equations, so they will be derived and discussed at length in section 3b below. We show below that the  $\xi$ s are functions of the vertical velocity at the TWI, the pressure slope of the TWI, the width of the CP, the horizontal pressure gradient force, and/or the drag coefficient.

### b. CP winds

As described by Kelly (1999), the continuity equations for the lower and upper sublayers of the layer of easterlies are

$$-u_B \Pi_B = \bar{\omega}_B \sigma_C - \bar{u}_+ \delta p_B, \quad (1)$$

$$-u_+ \Pi_+ = \bar{u}_+ \delta p_B - (\bar{\omega}_B - \bar{\omega}_L) \sigma_C, \quad (2)$$

where an overbar denotes a horizontal average across the CP region,  $\delta p_B$  is the pressure difference at the top of the TWI between the eastern and western boundaries of the CP region, and the wind speeds  $u_B$  and  $u_+$  are evaluated at the CP–WP boundary. Because the vertical velocity is assumed to be independent of height for  $p_L \leq p \leq p_B$ , the vertical velocities in the second term on the right hand side of (2) cancel. Adding (1) and (2) and solving for  $u_+$  yields

$$u_+ = \frac{-\bar{\omega}_B \sigma_C - u_B \Pi_B}{\Pi_+}. \quad (3)$$

This is a point at which our model diverges from

TABLE 1. Symbols used in the description of the model.

Symbol	Definition	Value
$\sigma, \sigma_w, \sigma_C$	Widths of the Pacific basin, WP, and CP	$1.5 \times 10^7$ m, calculated, calculated
$N_S, N_\infty$	Net surface, top-of-atmosphere (TOA) energy flux	Calculated
$T_{SW}, T_{SC}$	Mean SST in the WP and CP	Specified
$F_H, F_q$	Net atmospheric exchanges of energy and moisture between boxes, normalized by WP width	Calculated
$q_L, q_U$	Water vapor specific humidity entering/leaving the WP in the lower/upper troposphere	Calculated
$h_L, h_U$	Moist static energy entering/leaving the WP in the lower/upper troposphere	Calculated
IWP	Ice water path—vertically integrated cloud ice in the WP	Calculated
$\omega_L$	Subsidence rate at 600 mb in the CP	Calculated
$U_A$	Rate at which mass is pumped through the system	Calculated
$u_B$	Vertical-mean boundary layer wind speed at interface between WP and CP	Calculated
$q_{sw}$	Specific humidity at the surface of the WP region	Calculated
$\Pi_B, p_{BW}$	Pressure thickness/pressure level of trade wind layer/inversion	Prescribed

those of P95, M96, and LHK. In these three previous studies and in our study, the mass flux through the TWI is estimated based on the approximate balance between subsidence and radiative cooling in the Tropics. For P95 and M96, the pressure level of the TWI was assumed, and so the mean wind speed follows directly from the definition of mass flux given above. LHK calculated the

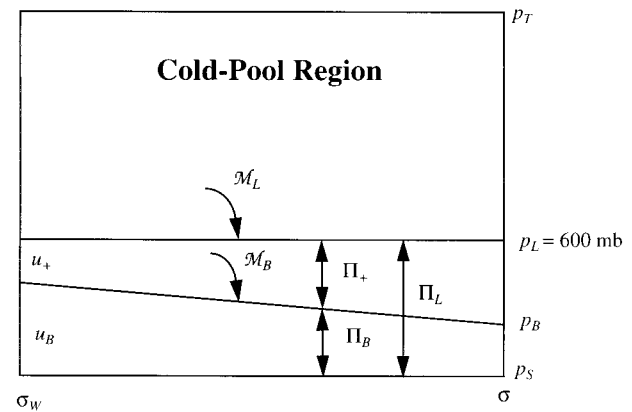


FIG. 3. Schematic illustrating the structure and terminology for the CP region of the atmosphere. Here  $p_L$  is the pressure level separating the lower and upper troposphere and at which the zero-wind level is assumed to occur;  $p_B$  is the pressure level at the top of the boundary layer;  $p_S$  is the surface pressure;  $M_L$  and  $M_B$  are the mass fluxes through  $p_L$  and  $p_B$ ;  $u_B$  and  $u_+$  are the zonal winds in the boundary layer and in the layer between  $p_L$  and  $p_B$ ;  $\sigma_w$  in this figure is the western border of the CP and  $\sigma$ , the eastern border.

TABLE 2. Governing equations of the CP.

Equation	Assumptions	Principle
$u_B = \frac{-\xi_2 - \sqrt{\xi_2^2 - 4\xi_1\xi_3}}{2\xi_1}$	Neglects momentum advection	Conservation of momentum
$(h_L - h_U)U_A = (N_{zC} - N_{sC})\sigma_C$	Moist static energy transported through convection from WP surface to CP SST specified; energy flux at surface implies ocean heat transports	Conservation of moist static energy
$(q_L - q_U)U_A = \Delta E_c \sigma_C$	Moisture export from CP defined by evaporation efficiency $\Delta$ Moisture export from WP determined by specified transport level, $p_{\min}$	Conservation of moisture
$\omega_L = g \frac{\delta R_F}{s_U - s_B}$	$\delta\omega/\delta p = 0$ in troposphere and $\omega = 0$ at the tropopause Simple radiative transfer scheme accounts for cooling due to water vapor	Thermodynamic energy
$U_A - M_L \sigma_C = 0$	Atmospheric circulation assumed to be closed	Mass continuity

pressure depth of the CPBL based on energy and moisture balance constraints. The vertical-mean wind speed in their model then follows from the mass continuity. Using values for the subsidence rate and the relative area of the CP for the base case of LHK, the implied vertical-mean wind speed in the CPBL at the CP–WP boundary is  $39 \text{ m s}^{-1}$ , which is very unrealistic. In our model, we compute the vertical-mean wind speed in the CPBL from a simplified momentum equation, which is explained below.

As discussed by Kelly (1999), momentum advection in the Tropics is an order of magnitude smaller than the other terms of the momentum equation, and so we neglect it. Considering an idealized circulation on the equator so that the Coriolis parameter is zero, we have

$$gM_B(u_+ - u_B) - \left\langle \frac{\partial\phi}{\partial x} \right\rangle \Pi_B + g\rho C_D u_B^2 = 0, \quad (4)$$

where  $x$  is the east–west coordinate,  $\phi$  is geopotential height,  $C_D$  is the drag coefficient,  $\rho$  is the density of air,  $g$  is the acceleration of gravity, and  $\langle \rangle$  represents a vertical average in the trade wind layer. The first term of (4) represents an acceleration due to the entrainment of air with velocity  $u_+$  into the trade wind layer. The second term is the vertical-mean horizontal pressure gradient force in the trade wind layer, while the last term is the surface wind stress. Here  $C_D$  was chosen to parameterize the surface stress in terms of the vertical-mean wind speed in the trade wind boundary layer. We found that  $C_D = 8.0 \times 10^{-4}$  gives reasonable results. Since we expect  $u_B < 0$ , we have set  $|u_B| = -u_B$  in the surface wind stress term of (4). This means that the model would break down if  $u_B$  ever became positive.

Under the assumption that the height of the TWI is steady (see KRS), the mass flux through the TWI,  $M_B$ , can be written as

$$gM_B = \omega_B - u_+ \frac{\partial p_B}{\partial x}. \quad (5)$$

Equation (5) states that in a time average, the net flux through the TWI due to turbulent entrainment is balanced by subsidence and horizontal advection.

Using  $u_L \Pi_L \equiv u_B \Pi_B + u_+ \Pi_+$  to eliminate  $u_+$  in (4) and (5), and (5) to eliminate  $M_B$  in (4), we obtain a quadratic equation for  $u_B$ . If the negative square root is taken to ensure that  $u_B$  is negative, the result is the momentum equation as written in Table 2, where for convenience, we have defined

$$\xi_1 \equiv g\rho C_D - \frac{\Pi_B/\Pi_+}{[1 - (\Pi_B/\Pi_+)]^2} \frac{\partial p_B}{\partial x}, \quad (6a)$$

$$\xi_2 \equiv \frac{-\omega_B}{[1 - (\Pi_B/\Pi_+)]} - \frac{[1 + (\Pi_B/\Pi_+)]}{[1 - (\Pi_B/\Pi_+)]^2} \frac{\partial p_B}{\partial x}, \quad (6b)$$

$$\xi_3 \equiv \frac{u_L \omega_B}{[1 - (\Pi_B/\Pi_+)]} - \frac{u_L^2}{[1 - (\Pi_B/\Pi_+)]^2} \frac{\partial p_B}{\partial x} - \left\langle \frac{\partial\phi}{\partial x} \right\rangle \Pi_B. \quad (6c)$$

Given the vertical-mean boundary layer pressure gradient, the vertical velocity at the TWI, and the pressure slope of the TWI, we can use the momentum equation to calculate  $u_B$ . As described later, the pressure gradient can be calculated as a function of the SST and pressure slope of the TWI, while the vertical velocity can be diagnosed as the subsidence rate needed to balance the free-tropospheric radiative cooling rate down the given lapse rate.

The sensitivities of the zonal wind speeds in layers  $\Pi_B$  and  $\Pi_+$  are examined in Figs. 4 and 5. The solid and dashed lines in Figs. 4 and 5 correspond to the left and right axes, respectively. The squares in each plot denote the estimated real-world value for the right-hand  $y$  axis, while the circles denote the real-world value for the left-hand  $y$  axis. As one would expect, the mean wind speed in the boundary layer increases as the slope of the TWI and the east–west SST difference increase. When the SST gradient vanishes,  $u_B$  does not tend to

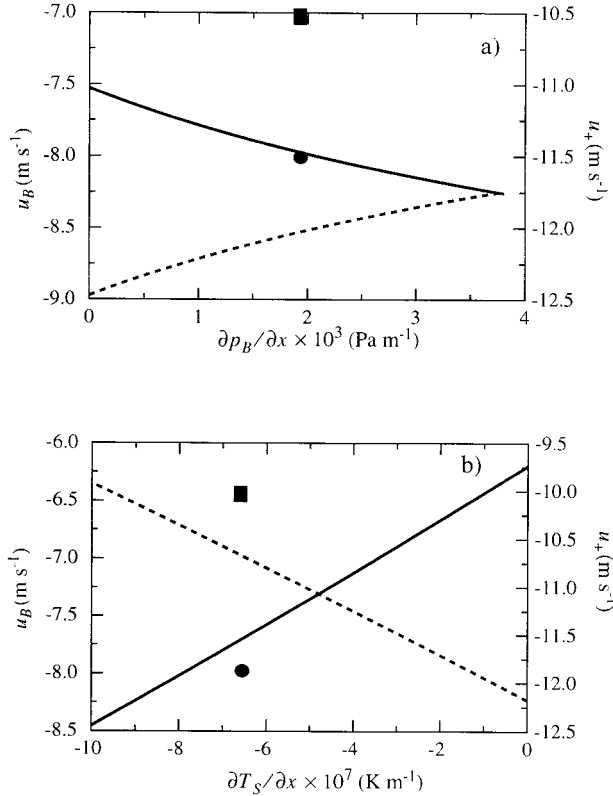


FIG. 4. The zonal winds in layer  $\Pi_B$  (solid line) and layer  $\Pi_+$  (dashed line) as functions of (a) the slope of the TWI ( $\times 10^3$ ) for an SST gradient of  $-6 \times 10^7$  K m<sup>-1</sup>, and (b) the SST gradient ( $\times 10^7$ ). In both cases  $\omega_L = 3.5 \times 10^{-2}$  kg m<sup>-2</sup> s<sup>-1</sup>. The dot and square represent the mean values of  $u_B$  and  $u_+$ , respectively, estimated from the observations. The solid and dashed lines correspond to the left and right vertical axes, respectively.

zero, because it depends on the vertical velocity, which is assumed to remain constant in these plots. We would expect the vertical velocity in nature to respond to changes of the SST gradient. Note also that  $u_B$  decreases by less than 1 m s<sup>-1</sup> as the slope of the TWI increases through the range depicted in Fig. 4. For this reason, we chose to specify the east–west pressure difference for the TWI.

By continuity, the wind speed in the upper sublayer of easterlies must decrease as  $u_B$  increases, if the mass flux through TWI remains constant. This is what we see in Fig. 4. Based on observations discussed by Hastenrath (1998), the mean wind speeds in each layer are estimated quite well. In Fig. 5, we see that the behavior of the winds with respect to vertical velocity and fractional width of the CP is complex. As a function of the vertical velocity, the wind in the TW layer,  $u_B$ , has a pronounced maximum near  $\omega_L = 0.015$  Pa s<sup>-1</sup>, for the given set of specified parameters. This maximum is due to the quadratic form of (4). As the fractional width of the CP increases, the SST gradient and gradient of TWI pressure level decrease (the east–west SST difference and east–

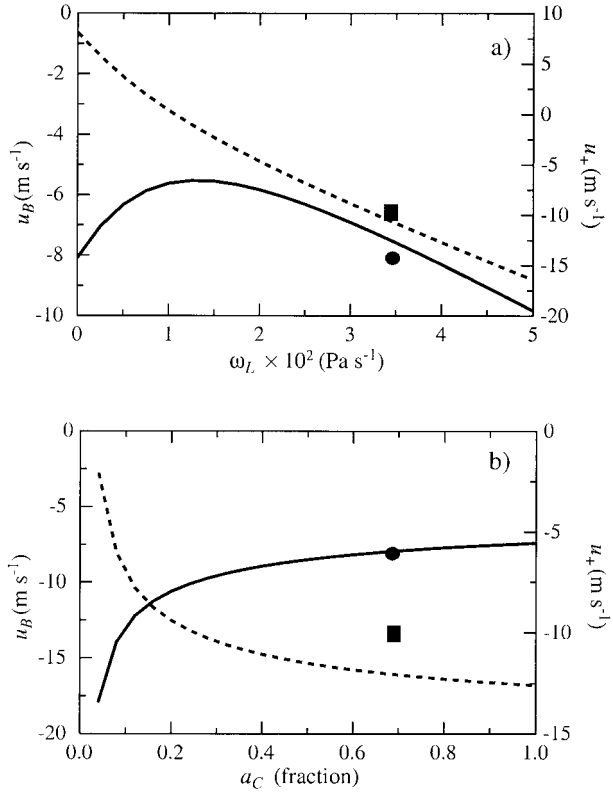


FIG. 5. The zonal winds in layer  $\Pi_B$  (solid line) and layer  $\Pi_+$  (dashed line) plotted as functions of (a) the vertical velocity at the top of the layer of easterlies for an SST gradient of  $-6 \times 10^7$  K m<sup>-1</sup>, and (b) the fractional width of the CP for an east–west SST difference of 6 K, an east–west difference in the top of the TWI of 200 mb, and  $u_L = 10$  m s<sup>-1</sup>. The dot and square represent the mean values of  $u_B$  and  $u_+$ , respectively, estimated from the observations. The solid and dashed lines correspond to the left and right vertical axes, respectively.

west TWI pressure level difference are specified), and so the boundary layer wind speed must also decrease.

Kelly (1999) showed that the mean boundary layer pressure gradient approximately satisfies

$$\left\langle \frac{\partial \phi}{\partial x} \right\rangle = \frac{1}{2\Pi_B} \frac{R}{p_s} \frac{\partial T_s}{\partial x}. \quad (7)$$

For a spatially uniform temperature gradient, (7) indicates that the pressure gradient force varies horizontally due to the variation of the boundary layer pressure depth and surface pressure. The magnitude of the pressure gradient force increases with the SST gradient. For  $\partial T_s / \partial x = -6.5$  K m<sup>-1</sup>,  $p_B = 800$  mb, and  $p_s = 1000$  mb, (7) gives a pressure gradient of  $1.9 \times 10^{-5}$  m<sup>2</sup> s<sup>-2</sup>; this compares well with  $-\langle \partial \phi / \partial x \rangle = -2.5 \times 10^{-5}$  m<sup>2</sup> s<sup>-2</sup>, which is a mean pressure gradient for the CP region as estimated from the ECMWF reanalysis dataset.

An additional simplification can be made. From (4), the mean CPBL pressure gradient is inversely proportional to the surface pressure  $p_s$ . The ECMWF reanalysis shows that the variation of surface pressure across the

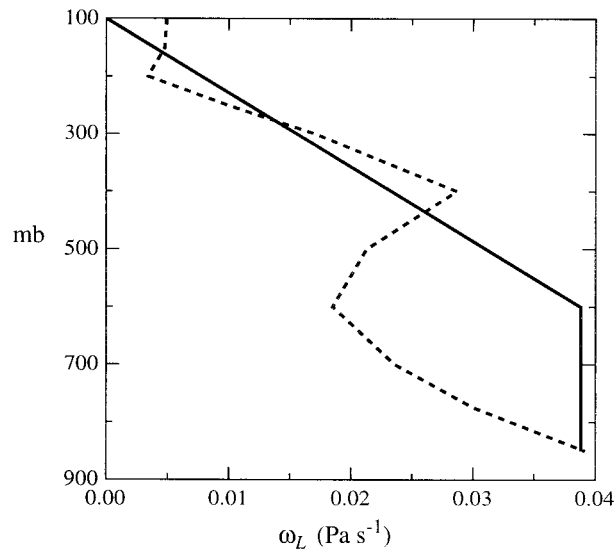


FIG. 6. Vertical velocity over the eastern, equatorial Pacific as a function of pressure. The dashed curve shows monthly mean values for Jan 1989 from the ECMWF reanalysis dataset. The solid curve shows values computed from the model's thermodynamic energy equation.

equatorial Pacific is less than 1%. Taking advantage of this small variation, we assume that  $p_s^{-1} \approx \bar{p}_s^{-1}$ , where in this case the overbar represents the zonal average for the CP. We assume that  $\bar{p}_s = 1003$  mb.

### c. CP subsidence

Following previous box studies (e.g., P95), we assume that the radiative cooling of the free troposphere is balanced by adiabatic compression and sinking. As described later, our radiation parameterization requires the vertically integrated water vapor as input, and returns the net radiative flux for the slice of the atmosphere over which the column water vapor was computed. Given the simplified nature of this radiation scheme, it does not seem prudent to compute the vertical velocity level by level for the CP free troposphere. Instead, we compute the radiative flux divergence for the free troposphere, and compute  $\omega_B$  for a simplified free-tropospheric divergence profile. Although we could assume that the vertical velocity is independent of height as in M97, it seems somewhat more realistic to assume that  $\partial\omega/\partial p$  is constant with height in the upper troposphere. Assuming that  $\omega = 0$  at the tropopause,  $\partial\omega/\partial p$  is constant in the upper troposphere, and  $\partial\omega/\partial p = 0$  in the lower troposphere, we can derive the thermodynamic energy equation given in Table 2, based on the observed balance between the radiative cooling rate and adiabatic compression/sinking.

For a typical moisture and temperature profile from the ECMWF reanalysis dataset, we have computed the profile of  $\omega$  using the thermodynamic energy equation. We calculated the radiative fluxes in the thermodynamic

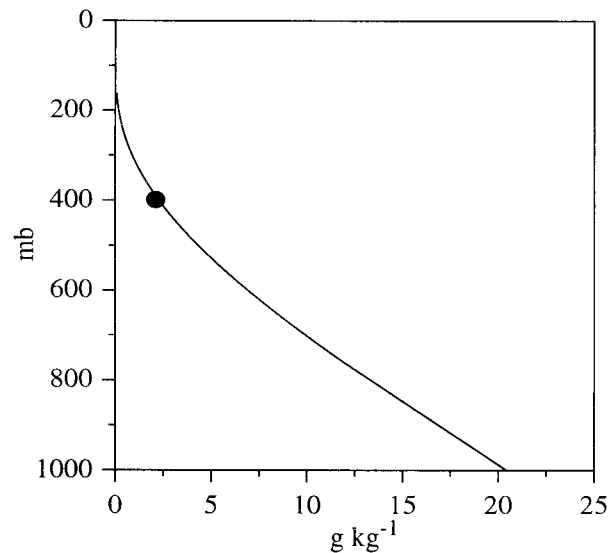


FIG. 7. The specific humidity profile which results for  $T_{sw} = 302$  K,  $W = 65$  kg m<sup>-2</sup>, and RH = 80%. The black dot represents the effective pressure level from which the free-tropospheric mass flux transports water vapor.

energy equation from the National Center for Atmospheric Research's Community Climate Model version 3 radiation code using ECMWF temperature and moisture profiles as input. Figure 6 shows that the monthly mean vertical velocity profile from the ECMWF reanalysis dataset (dashed curve) and the vertical velocity profile obtained using the thermodynamic energy equation (solid curve) agree fairly well in the mid- and upper troposphere. Our parameterization overestimates the vertical velocity by 100% as compared with the ECMWF reanalysis dataset at lower levels, but slightly underestimates the subsidence rates in comparison with Betts and Ridgeway (1989) and LHK.

### d. CP budgets

A derivation of the moist static energy budget (Table 2) is given in appendix A. We determine the left-hand side of the moist static energy budget independently of the right-hand side. Here  $U_A$  is known, and  $h_L$  and  $h_U$  can be calculated. The quantity  $h_L$  is the mass-weighted vertical-mean moist static energy in the layer of easterlies, which is exported to the WP, and  $h_U$  is the moist static energy in the upper troposphere of the WP region, which is exported to the CP. Under the assumption that convecting parcels in the WP originate from near the surface,  $h_U \equiv c_p T_{sw} + Lq_{sw}$ , where  $q_{sw}$  refers to the specific humidity at the surface in the WP region. We calculate the lateral energy transport in the lower-tropospheric layer as  $U_A h_L$ . The quantity  $h_L$  may be explicitly calculated given the lapse rate in the CPBL, the temperature at the base of the layer, and water vapor content. The mean lapse rate in the CPBL is assumed to satisfy  $\Gamma_B = \Gamma_d(1 - \text{RH}) + \Gamma_{ms}(\text{RH})$ , where  $\Gamma_d$  is

the dry adiabatic lapse rate,  $\Gamma_{ms}$  is the moist adiabatic lapse rate at the surface, and RH is the surface relative humidity. The moisture contribution of the moist static energy is  $Lq_L\Pi_Lg^{-1}$ , where  $q_L$  is the mass-weighted vertical-mean specific humidity in the CPBL. If we divide the moist static energy equation by  $\sigma_w$ , then the left hand side is equivalent to  $F_H$ , the lateral heat exchange, which is defined later [see Eq. (13)].

A derivation of the moisture budget (Table 2) is given in Kelly (1999). We have specified an evaporation efficiency, and so  $\Delta$  is the fraction of the evaporated water vapor that is available for export to the WP. Without accounting for CP precipitation in some way, the amount of water vapor exported to the WP in this model is too large. The overabundance of water vapor can partially be explained by our assumption of a closed circulation in the atmosphere. Rainfall in the CP seems to be related to incursions of the ITCZ or to passage of transitory waves such as the Madden–Julian oscillation. Our assumption of an evaporation efficiency provides a crude mechanism for exploring the effect of precipitation in the CP on the zonal circulation in the equatorial atmosphere. It can be shown that  $F_q$  is proportional to the net evaporation rate in the CP.

If we specify the vertical variation of relative humidity and zonal wind at the CP–WP boundary, then we can compute  $q_U$  from

$$q_U = g^{-1}U_A^{-1} \int_{\Pi_U} uq dp$$

and estimate the pressure level to which  $q_U$  corresponds. Figure 7 shows an example for which the zonal wind decreases linearly to zero at the TWI from its maximum at the tropopause and the relative humidity is independent of height. Under these conditions,  $q_U = 2.5 \text{ g kg}^{-1}$ , which for the given relative humidity profile, implies that the effective level from which  $U_A$  transports water vapor is approximately 400 mb. This effective transport level is not very sensitive to lapse rate variations, which in turn depend on the WP SST, precipitable water, and cloud cover. For SST = 302 K and  $\partial T_s/\partial x = -6.4 \times 10^{-7} \text{ K m}^{-1}$ , the effective water vapor transport level increases by 25 mb as the precipitable water decreases by  $20 \text{ kg m}^{-2}$ . For  $W = 55 \text{ kg m}^{-2}$  and  $\partial T_s/\partial x = -6.4 \times 10^{-7} \text{ K m}^{-1}$ , the effective water vapor transport level increases by 5 mb as the SST decreases by 4 K. For SST = 302 K and  $W = 55 \text{ kg m}^{-2}$ , the effective transport level increases by 23 mb and decreases by 10 mb as the SST gradient is doubled and halved, respectively. Given its relatively small sensitivity to the model variables, we calculate  $q_U$  based on an assumed fixed effective transport level.

For the box model, we obtain the relative humidity at the WP surface from a surface humidity assumption, which relates the surface relative humidity to the column water vapor, and then assume that the relative humidity is independent of height in the troposphere. The as-

sumption that relative humidity is independent of height is in broad agreement with observations during convectively active periods during the Tropical Ocean and Global Atmosphere Coupled Ocean–Atmosphere Response Experiment (Brown and Zhang 1997). The surface humidity assumption (described in detail in KRS) relates the surface relative humidity to the ratio of the column water vapor and the saturation column water vapor, that is, the column water vapor that would exist if the entire column were saturated. This assumption allows us to use precipitable water as an independent variable, rather than specific humidity. The precipitable water is not very dependent on the vertical profile of relative humidity in the upper troposphere, because most of the water vapor resides near the surface.

We assume that the mean evaporation rate can be determined by using the arithmetic average of the zonal wind speeds at the east and west boundaries of the CP in the bulk parameterization for evaporation. We assume, based on the ECMWF reanalysis, that the surface relative humidity in the interior of the CP region is similar to that in the WP region. As described above, the wind speed, surface temperature, surface pressure, and vertical-mean specific humidity of the CPBL are required in order to calculate the evaporation rate.

It remains to relate the surface evaporation rate to boundary layer wind  $u_B$ , which is diagnosed by the model. We simply specify the transfer coefficient  $c_T$  so as to compute the evaporation rate from the mean boundary layer wind speed rather than from the 10-m wind (Deardorff 1972). We specify the heat transfer coefficient to be  $c_T = 8.0 \times 10^{-4}$ . The computation is based on the relative humidity  $\text{RH} = q_c/q_{\text{sat}}(T_{SC}, p_{SC})$ , where  $q_c$  is the near-surface specific humidity and  $q_{\text{sat}}(T_{SC}, p_{SC})$  is the saturation specific humidity defined by the surface pressure and  $T_{SC}$ . Here RH has been assumed to be the same as that in the WP and the air–sea temperature difference has been neglected. The mean evaporation rate follows as

$$E_C = c_T \max(|u_B|, u_{\min})q_{\text{sat}}(T_{SC}, p_{SC})(1 - \text{RH})\rho, \quad (8)$$

where  $u_{\min}$  is the zonal wind speed on the eastern boundary of the CP. We specify  $u_{\min} = 3 \text{ m s}^{-1}$  for the purpose of calculating the mean evaporation rate.

To very good approximation, the specific humidity of the air in the mid- and upper troposphere is conserved as it traverses the equatorial Pacific Ocean (Salathé and Hartmann 1997). East of  $100^\circ\text{W}$ , the specific humidity of the air at mid- and upper levels increases as it moves eastward. This moistening occurs due to meridional exchanges and convection near the South American coast. We ignore meridional exchanges and convective processes in the CP, assuming instead that the air continues to subside there. Extremely low relative humidities and specific humidities would be expected at low levels just above the TWI if these moistening processes could be suppressed.

We therefore assume that the precipitable water in the CP follows from the water vapor profile in the WP. As

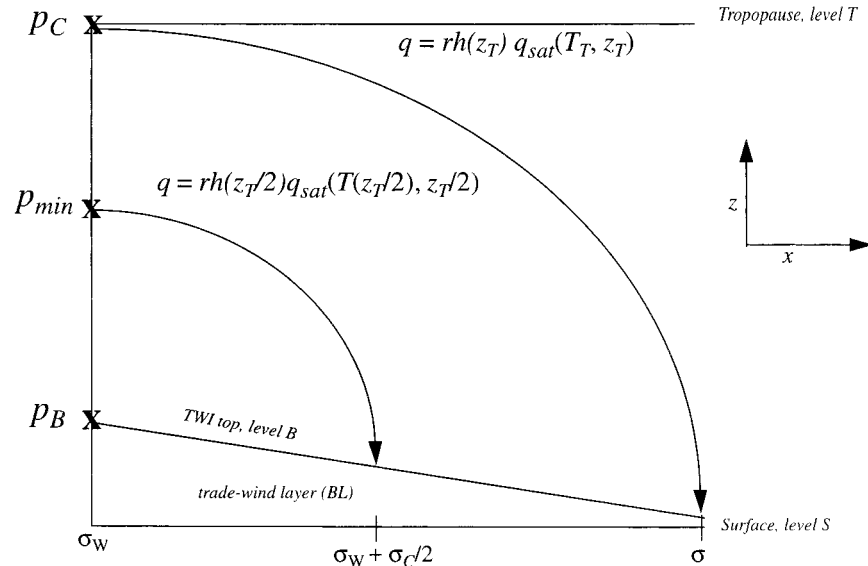


FIG. 8. Schematic illustrating the advection model for water vapor in the CP region ( $p_B$  is the pressure level at the top of the boundary layer;  $p_{\min}$  is the minimum advection pressure level;  $p_C$  is the pressure at the top of the convective layer;  $\sigma_w$  in this figure is the western border of the CP and  $\sigma$ , the eastern border).

shown in Fig. 8, the vertical specific humidity profile of the WP for the model rotates to become the horizontal specific humidity profile just above the CP TWI. The amount of water vapor in the CP then follows from the amount of water vapor in the WP column above the altitude from which the air was advected. For example, suppose that the outflow profile in the WP is such that air just above the TWI in the CP was advected from 500 mb and above. Then the precipitable water in the CP can be calculated by integrating the WP moisture profile from 500 mb to the tropopause. We refer to this level as the minimum advection level ( $p_{\min}$ ). The minimum advection level is equivalent to the effective water vapor transport level described above only if the zonal wind is uniform with height. Because air advected from 400 mb and above does not result in large enough values of precipitable water to achieve realistic radiative cooling rates,  $p_{\min}$  must be at a lower altitude than the effective water vapor transport level. We choose to set  $p_{\min} = 500$  mb. The solution is not very sensitive to the choice of effective water vapor transport level, because the main source of water vapor in the CPBL is evaporation not vertical advection. The solution is however highly sensitive to the choice of  $p_{\min}$ , since the radiative cooling rate depends on the precipitable water. Later we examine the sensitivities of our results to this assumption. Our approach is based on the assumption that advection controls the specific humidity of the CP free troposphere; in this respect we are following Salathé and Hartmann (1997).

#### e. CP radiation

Just as in KRS, we parameterize the net clear-sky longwave radiation at the top of the atmosphere (TOA)

and surface in terms of the surface temperature and precipitable water. These parameterizations are based on the findings of Stephens et al. (1994), who related the longwave radiation flux at the surface and TOA to SST and precipitable water. It is convenient to use this parameterization in our model, because it is simple and relatively accurate but does not depend on the details of the water vapor profile. The climatological relationships retrieved by Stephens and colleagues do, of course, implicitly depend on the vertical distribution of water vapor,  $\text{CO}_2$ , and other greenhouse gas absorbers, but we do not have to concern ourselves with these details.

Although the climatological relationships between radiative fluxes and SST and precipitable water provide longwave fluxes at the top and bottom of the atmosphere, they do not give the net fluxes in the free troposphere. We need the net fluxes in the free troposphere in order to calculate the subsidence rate in the CP region. In keeping with our philosophy of maximum simplicity, we continue our reliance on idealized methods for the calculation of the radiative cooling rate in the CP region. It would actually be easier to use an existing GCM-style radiative transfer parameterization. However, given the simplified treatment of the vertical profiles of relative humidity and temperature in our model (and in other box models), it seems inappropriate to use a detailed radiative transfer parameterization. The following section describes how we diagnose the longwave radiative cooling rate in the free troposphere.

In order to compute the radiative cooling rate of the free troposphere, we write the clear-sky longwave fluxes at the TOA and surface as

$$R_{z,\text{clr}} = \sigma T_{SC}^4 (1 - \varepsilon_B^+) (1 - \varepsilon_F^+) + \sigma T_E^4 \varepsilon_B^+ (1 - \varepsilon_F^+) + \sigma T_F^{+4} \varepsilon_F^+ \quad (9a)$$

$$R_{S,\text{clr}} = \sigma T_{SC}^4 - \sigma T_E^4 \varepsilon_B^- - \sigma T_F^{-4} \varepsilon_F^- (1 - \varepsilon_B^-), \quad (9b)$$

respectively. Here,  $\varepsilon$  refers to the emissivity, the subscripts  $B$  and  $F$  refer to quantities associated with the boundary layer and free troposphere, respectively, and the superscripts  $+$  and  $-$  denote quantities associated with upward and downward fluxes, respectively. For example,  $\varepsilon_F^-$  refers to the downward emissivity in the free troposphere. In general, the upward and downward emissivities of the free troposphere and boundary layer differ (Rodgers 1967). We assume for simplicity that  $T_E$ , the emission temperature of the boundary layer, is the arithmetic mean of temperatures at the top and bottom of the boundary layer. The emissivities can be evaluated, as described below. Because the left-hand sides can be computed (using the radiation parameterization described in KRS), we can solve for  $T_F^+$  and  $T_F^-$ , which are the upward and downward emission temperatures of the free troposphere.

Neglecting shortwave absorption, the radiative cooling rate of the free troposphere follows as

$$\delta R_F = \varepsilon_F^+ \sigma T_F^{+4} + \varepsilon_F^- \sigma T_F^{-4} - \varepsilon_F^+ [\sigma T_{SC}^4 (1 - \varepsilon_B^+) + \sigma T_E^4 \varepsilon_B^+]. \quad (10)$$

We neglect the effect of CPBL clouds on the radiative cooling of the free troposphere, because they have only a marginal effect (Stephens and Webster 1979). The clear-sky emissivity for the CP region is parameterized as

$$\varepsilon_{F,B}^\pm = \sum_{i=1}^4 (a_i^\pm \log W_{F,B})^i, \quad (11)$$

where the coefficients  $a_i$  are described in Rodgers (1967) and  $W_F$  and  $W_B$  are vertically integrated water vapor in the free troposphere and CPBL, respectively.

Plots of the emissivity as a function of water vapor are shown in Rodgers (1967) and in Stephens and Webster (1979).

Following Lacis and Hansen (1974), the transmissivity of shortwave radiation through the atmosphere is calculated as a function of  $W_C = W_F + W_B$ , the precipitable water in the CP, and on the solar zenith angle.

#### 4. WP model

The model of the WP region is similar to that described in KRS and is described in detail there. We give only a brief description here, focusing on the differences in the newer version. Refer to Table 1 for a description of the variables used. The model includes an explicit moisture budget, a simple convection parameterization, a simple but physically based radiation parameterization, and interactive clouds. The underlying surface is assumed to be ocean of specified SST. The independent variable is the vertically integrated water vapor content. The clear-sky longwave radiative fluxes are calculated as functions of SST and precipitable water, based on the methods described in Stephens and Greenwald (1991). In our simplified treatment of shortwave radiation, the only absorbers of shortwave radiation are stratospheric ozone and tropospheric water vapor. The lower-tropospheric lapse rate and surface evaporation rate are determined as functions of the SST and precipitable water. Cloud optical depth is parameterized as a function of ice water path, which in turn is a function of SST and precipitable water. Clouds reflect in the shortwave and emit and absorb in the longwave. A stratosphere in radiative equilibrium limits the depth of the convective layer.

The hydrological cycle has been generalized (relative to KRS) to include the effects of sublimation on the WP water vapor budget. As discussed in appendix B the steady-state solution for ice water path (IWP) is

$$\text{IWP} = \frac{\chi P - \frac{c}{t_s} + \sqrt{(\chi P)^2 + \left(\frac{c}{t_s}\right)^2 - \frac{2\chi c P}{t_s} + 4\left(\frac{1+\chi}{t_{\text{prec}}} + \frac{1}{t_s}\right)\left(\frac{1+\chi}{t_{\text{prec}}}\right)c^2}}{2\left(\frac{1+\chi}{t_{\text{prec}}} + \frac{1}{t_s}\right)} \quad (12)$$

if the effects of sublimation and cloud fraction are included in a simple way. Here  $c$  represents the value of IWP for which the cloud fraction is 0.5,  $\chi$  is a nondimensional parameter discussed in KRS,  $t_{\text{prec}}$  is an autoconversion timescale for the removal of ice by stratiform precipitation, and  $t_s$  is a timescale for the sublimation of cloud ice.

Figure 9 shows that IWP increases with WP SST ( $T_{sw}$ ) and decreases with WP precipitable water ( $W_w$ ) for fixed lateral moisture and energy transports in the WP. The precipitation rate was calculated from  $P_w = E_w + F_q$ , where  $E_w$  is the evaporation rate calculated from the bulk formula and  $F_q$  is the vertically integrated moisture convergence. A surface humidity assumption

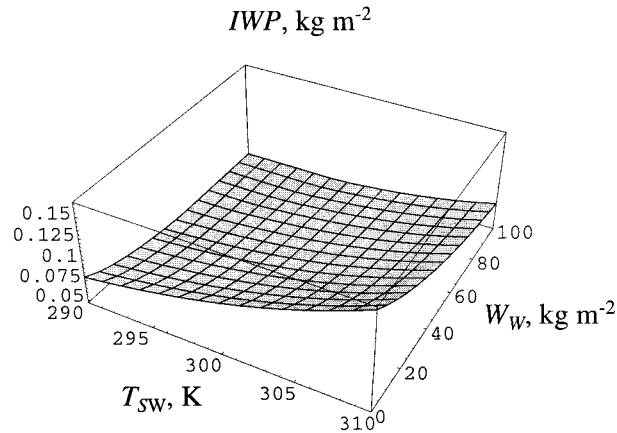


FIG. 9. IWP computed from (12) as a function of WP SST and precipitable water.

described in KRS and used here, relates the surface specific humidity to the column water vapor, and so  $E_w$  is a function of  $T_{sw}$  and  $W_w$ . For this plot, we chose  $t_{prec} = 1000$  s and  $t_s = 21\,600$  s (6 h), neglected the vertically integrated water vapor convergence in the WP, assumed that  $c = 0.05$  kg m $^{-2}$ , and specified the surface wind to be  $5$  m s $^{-1}$ . Note that the specified timescale for sublimation is much longer than that for stratiform precipitation. From our surface humidity assumption, the relative humidity of the near-surface air decreases as the SST increases and precipitable water decreases, and so the evaporation rate increases. This produces a larger precipitation rate, and from (12), increases the IWP. Because  $f$  is assumed to depend on IWP [(B4) in appendix B], the dependence of fractional cloudiness on  $T_{sw}$  and  $W_w$  is similar to that of IWP.

Figure 10 presents cloud fraction, precipitable water, and net radiative flux at the top of the atmosphere, respectively, for the WP and as functions of  $t_{prec}$ , the specified timescale for the autoconversion of cloud ice to snow, for three simulations performed with the WP model in stand-alone mode. We have assumed a surface wind speed of  $5$  m s $^{-1}$ ,  $T_{sw} = 300$  K, and a lateral latent heat flux of  $100$  W m $^{-2}$  into the WP column. In the first case, the cloud fraction was specified as  $0.7$  (solid line). In cases two and three, the cloud fraction and IWP were calculated from (B4) and (12), respectively. In order to demonstrate the effects of our sublimation parameterization, we set  $t_s \rightarrow \infty$  for case two and  $t_s = 6$  h for case three. As can be seen from the plot, the cloud fraction  $f$  increases as  $t_{prec}$  increases for cases two and three. As discussed in KRS,  $t_{prec}$  represents the timescale for removal of cloud ice by stratiform precipitation. As  $t_{prec}$

increases, the residence time for cloud ice in the atmosphere increases, and so the IWP is in equilibrium for larger values. As discussed in appendix B, the cloud fraction is parameterized to increase as IWP increases, and so  $f$  must increase as  $t_{prec}$  increases. Fractional cloudiness ranges from near  $f = 0.65$  for  $t_{prec} = 1000$  s to near  $f = 0.85$  for  $t_{prec} = 5000$  s for case two. The effect of sublimation in our model is to reduce the cloud fraction in comparison with case two. The sublimation-induced decrease in cloud fraction becomes more pronounced as  $t_{prec}$  increases.

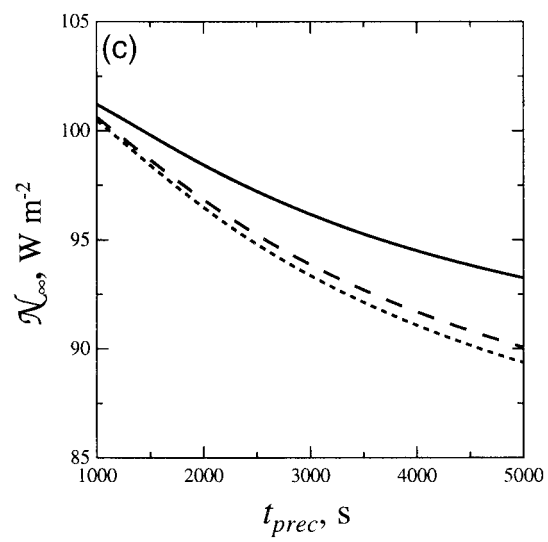
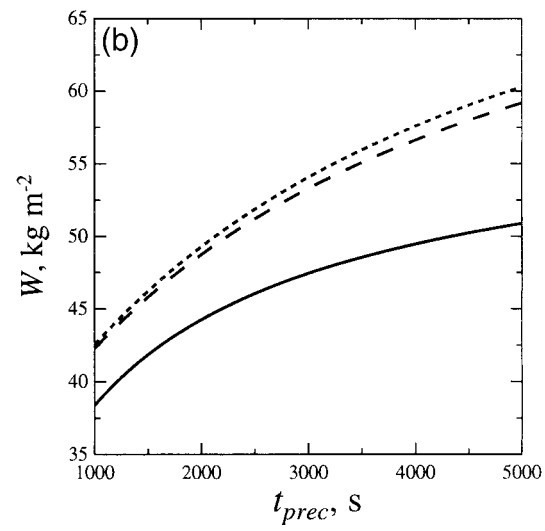
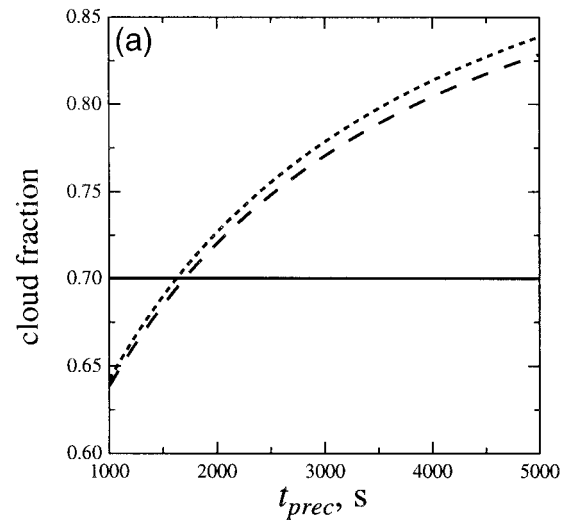
Figure 10 also demonstrates that calculating instead of specifying the cloud fraction can affect the net radiative balance at the top of the atmosphere. As the cloud fraction increases, the shortwave flux at the surface decreases. The increased precipitable water for cases two and three (relative to case one) increases the opacity of the atmosphere to longwave radiation. As a result, the net longwave radiative flux at the surface decreases and therefore compensates for the weaker shortwave energy input at the surface. The radiative effects of the cloud and the precipitable water combine to reduce the net radiative flux at the TOA, as compared with case one. The albedo effect becomes slightly more intense with the cloud fraction being computed rather than specified. The net downward energy flux at the TOA decreases by  $1$  W m $^{-2}$  for  $t_{prec} = 1000$  s and decreases by only  $5$  W m $^{-2}$  for  $t_{prec} = 5000$  s, as compared with the case with fixed cloud fraction. The net flux at the TOA ranges between  $100$  and  $90$  W m $^{-2}$ , which is quite realistic. These results illustrate a sensitivity of the net cloud forcing (relative intensities of the albedo effect and greenhouse effect) to  $t_{prec}$ , which was described in detail by KRS. These results do not address the sensitivity of the net cloud radiative forcing to changes of cloud fraction. Although the curves cross in Fig. 10a near  $t_{prec} = 1500$  s, the solutions differ because the cloud optical depths differ.

## 5. Coupling of the CP and WP atmospheres

Up to this point, we have been discussing the energy and moisture balance equations for the CP and WP separately. However, for equilibrium to exist, the two-box system must be in energy and moisture balance.

The major differences between KRS and the present study are that the wind stress and lateral heat and moisture exchanges between WP and CP are now calculated. The lateral heat and moisture exchanges between the WP and CP are defined as

FIG. 10. Plots of (a) cloud fraction, (b) precipitable water, and (c) net radiative flux at the top of the atmosphere as functions of  $t_{prec}$ , the timescale for autoconversion of cloud ice to snow. For the first case, the cloud fraction (solid line) was specified; for the second case, the cloud fraction was calculated, but the effects of sublimation were neglected (dashed line); for the last case, the effects of sublimation were included in the calculation (dotted line).



$$F_H \equiv \frac{U_A(h_L - h_u)}{\sigma_w}, \quad (13a)$$

$$F_q \equiv \frac{U_A(q_L - q_u)}{\sigma_w}. \quad (13b)$$

In defining (13), we have assumed that  $u_B$  vanishes at the western boundary of the WP, and so the vertically integrated flux divergence of moist static energy and latent heat are determined by the flow at the eastern boundary of the WP.

Energy and moisture balance for the Walker circulation are given by

$$\sigma_C(N_{\infty C} - N_{SC}) + \sigma_w(N_{\infty W} - N_{SW}) = 0, \quad (14a)$$

$$\sigma_C \Delta E_C + \sigma_w(E_W - P_W) = 0, \quad (14b)$$

where  $\Delta$  is an evaporation efficiency that specifies the proportion of evaporated water vapor that is exported to the WP region. Using the definitions (13a) and (13b) in the moist static energy and moisture budgets (in Table 2), respectively, and substituting the results in (14a) and (14b) to eliminate the WP quantities, we have

$$\sigma_C(N_{\infty C} - N_{SC}) - \sigma_w F_H = 0, \quad (15a)$$

$$\sigma_C \Delta E_C - \sigma_w F_q = 0. \quad (15b)$$

We need not consider (15b) further, because we have shown previously that  $F_q$  is derived directly from the mean evaporation rate for the CP. Thus (15b) is identically satisfied. As discussed previously in section 3d,  $F_H$  is derived independently of the atmospheric energy balance for the CP, and so (15a) is not automatically satisfied. It can thus be used as a constraint on the system, which we can use to compute  $\sigma_w$ .

Dividing through by  $\sigma$ , recalling that  $a_w + a_c = 1$ , and defining  $a_w = \sigma_w/\sigma$  and  $a_c = \sigma_C/\sigma$ , (14a) may be rewritten as

$$a_c = \left[ 1 - \frac{(N_{\infty C} - N_{SC})}{(N_{\infty W} - N_{SW})} \right]^{-1}. \quad (16)$$

Although (16) gives us a method to solve for  $a_c$  directly, the evolution of the system to equilibrium is much smoother if we treat the time rate of change of  $a_c$  as a relaxation process. Hence, we assume that the fractional width of the CP evolves according to

$$\frac{a_c - a_c|_0}{\Delta t} = \frac{a_c^* - a_c|_0}{t_{ac}}, \quad (17)$$

where  $a_c$  is the new value,  $a_c|_0$  is the fractional width obtained from (16),  $a_c^*$  is the fractional width from the previous time step,  $t_{ac}$  is a time scale for the relaxation process, and  $\Delta t$  is the time step.

Equilibria of the system were obtained numerically using a simple time-marching procedure. The method of solution is as follows. Under the assumption that the energy and hydrological cycles of the atmosphere adjust

rapidly compared to the fractional widths of the WP and CP, the WP model is integrated in time until an equilibrium is found. Because the ocean mixed layer is assumed to be infinitely deep, SST in the WP and CP cannot change. After the WP has equilibrated, a new value for  $a_c$  is computed and then compared with the current value. If the difference between these values is small (and the atmosphere is energetically balanced to within  $0.1 \text{ W m}^{-2}$ ), the solution is accepted. If not, then a new value of  $a_c$  is computed from (17), and the process is repeated. The goal is to find a solution in which the time rates of change are small for WP precipitable water, and fractional widths of the CP and WP. The solution occurs for the fractional widths of the CP and the WP in which the mean surface energy flux for the Walker circulation is balanced by the mean TOA energy flux for the Walker circulation. Characteristics of the solution are discussed in the next section. As mentioned before, the ‘‘time-dependent’’ behavior has no meaning; only the equilibria will be discussed.

## 6. Tests of the CP model

As discussed earlier, we specify the minimum pressure ( $p_{\min}$ ) level from which water vapor from the WP troposphere can moisten the interior of the CP region. Because air traversing the CP free troposphere sinks, water vapor that emerges from the lower troposphere would not travel far before subsiding through the TWI. The value of  $p_{\min}$  depends on the vertical structure of the Walker circulation, the meridional Hadley circulation, and the frequency of deep convection. A series of runs described in the next paragraph are designed to illustrate the sensitivity of the circulation in our model to  $p_{\min}$ . For each of these runs,  $T_{SW} = 303 \text{ K}$ ,  $T_{SE} = 296 \text{ K}$ , and  $W_w = 50 \text{ kg m}^{-2}$ .

Figure 11 shows how the circulation changes as  $p_{\min}$  varies. As  $p_{\min}$  increases from 400 to 700 mb, the precipitable water in the CP free troposphere increases from 3 to 13  $\text{kg m}^{-2}$  (Fig. 11a). As the precipitable water increases, so does the radiative cooling rate. Because subsidence approximately balances radiative cooling, the subsidence rate must increase as the radiative cooling rate increases, which is what we see in the figure. Consistent with the enhanced subsidence rate, the mass flux also increases with the  $p_{\min}$ . Because we have fixed the SST and the fractional widths of the WP and CP for this plot,  $F_H$ , the lateral energy flux, must increase as  $p_{\min}$  increases. As we see from Fig. 11b,  $F_H$  increases from 25 to 200  $\text{W m}^{-2}$  through the specified range of  $p_{\min}$ . For the two-box model, the SST or precipitable water difference between the CP and WP would have to decrease in order to balance  $F_H$  with the vertical energy flux divergence of the CP atmosphere. Our model assumes that the width of the CP adjusts so as to achieve this balance. In nature, SST could also vary.

The mechanism identified in the preceding paragraph suggests a feedback. As discussed in KRS, the tropo-

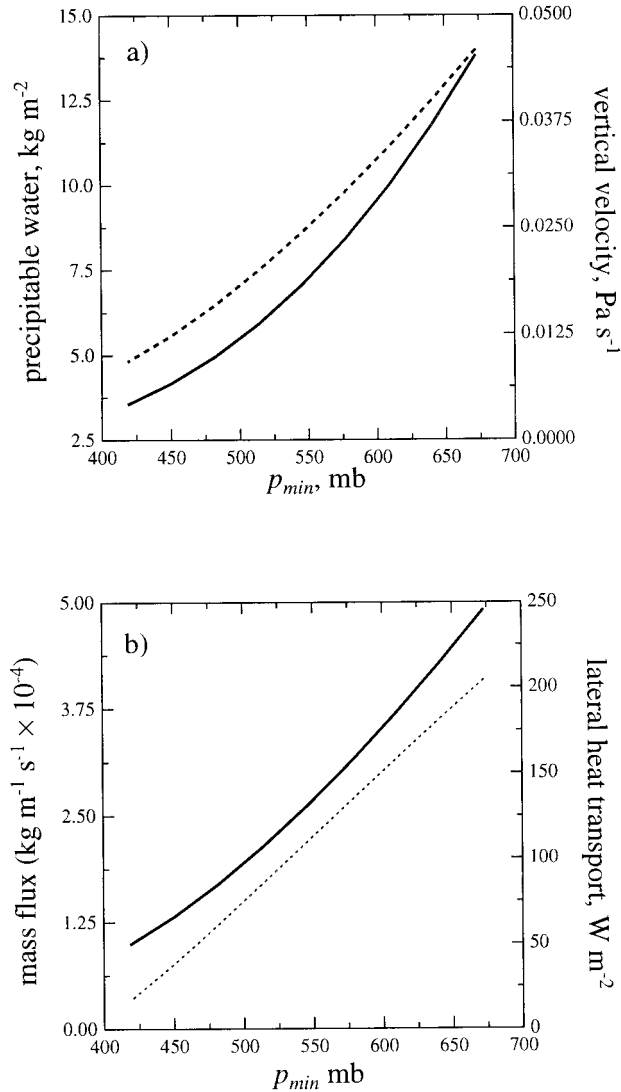


FIG. 11. Stand-alone results for the CP atmosphere. For these simulations, SST in both regions and precipitable water in the WP region were specified. The value of  $p_{min}$  was varied. In each of these panels, the solid and dotted lines are associated with the left and right axes, respectively. (a) Precipitable water (solid line) and vertical velocity at the TWI (dotted line); (b) the mass flux (solid line) and lateral energy transport (dashed line) associated with the Walker circulation.

pause height and temperature increase and decrease, respectively, as the surface temperature, precipitable water, and/or cloud fraction in the WP region increase. As a result, the air which is transported laterally from the upper troposphere of the WP to the CP will be drier where the tropopause is higher. As shown in Fig. 11a, drier air would have a smaller vertical velocity and hence would slow the circulation. This is similar to a feedback mechanism proposed by Lindzen (1990). We return to this point later.

**7. Results**

Table 3 presents the results for our base case. Based on data from ECMWF reanalyses, we have specified  $T_{sw} = 303 \text{ K}$  and  $T_{se} = 296 \text{ K}$ . As shown in Table 3, the values of the precipitable water in the WP and CP are 53.8 and 18.1  $\text{kg m}^{-2}$ , respectively,  $F_q = 110 \text{ W m}^{-2}$ , and  $F_H = -57.4 \text{ W m}^{-2}$ . For the lateral heat transports, a positive value indicates a net transport of energy from the CP to the WP. In KRS,  $F_q$  and  $F_H$  were prescribed based on observational estimates as 100  $\text{W m}^{-2}$  and  $-60 \text{ W m}^{-2}$ , respectively, so transports simulated by this model for the base case are quite realistic. The precipitable water values simulated for the rising and sinking branches of the zonal circulation are quite realistic as compared with a 10-yr SSM/I satellite dataset (Fig. 12). In particular, the precipitable water in convecting zones of the tropical Pacific Ocean (the WP and South Pacific convergence zone) is larger than 50  $\text{kg m}^{-2}$ ; in the tropical eastern Pacific, strong subsidence and infrequent convection result in precipitable water less than 20  $\text{kg m}^{-2}$  over a large area.

To further understand the sensitivities of our model, consider Fig. 13. Figure 13a presents the equilibrium values of precipitable water and WP fractional width as functions of  $T_{se}$ . Unless stated otherwise,  $T_{sw} = 303 \text{ K}$ . As can be seen from the figure,  $a_w$  increases at a moderate rate from near 0.01 for  $T_{se} = 292 \text{ K}$  to near 0.2 for  $T_{se} = 296 \text{ K}$ . Within this  $T_{se}$  interval, the precipitable water,  $W_w$ , decreases by less than 2  $\text{kg m}^{-2}$ . As  $T_{se}$  increases from 296 to 300 K, both  $a_w$  and  $W_w$  increase strongly. Here  $F_q$  and  $F_H$  steadily decrease and

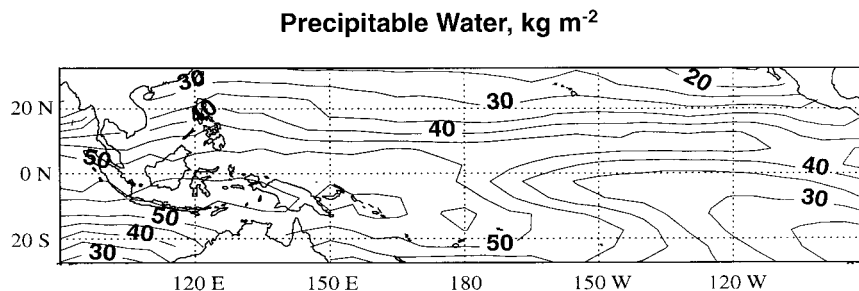


FIG. 12. Contour plot of precipitable water ( $\text{kg m}^{-2}$ ) from SSM/I satellite observations for an average of Jan between 1988 and 1991. The contour interval is 5  $\text{kg m}^{-2}$ .

TABLE 3. Base case results.

Variable	Fixed SST	Mixed layer SST
Fractional width of the WP ( $a_w$ )	0.207	0.127
$W_w$	53.8 kg m <sup>-2</sup>	55.6 kg m <sup>-2</sup>
$T_{sw}$	303 K	305.3 K
$W_c$	18.1 kg m <sup>-2</sup>	18.7 kg m <sup>-2</sup>
$T_{se}$	296 K	298.5 K
Maximum vertical-mean zonal wind in the CPBL	-5.6 m s <sup>-1</sup>	-5.4 m s <sup>-1</sup>
Surface latent heat flux in CPBL	112.3 W m <sup>-2</sup>	137.2 W m <sup>-2</sup>
Lateral moist static energy transport ( $F_H$ )	-57.4 W m <sup>-2</sup>	-80.7 W m <sup>-2</sup>
Lateral latent heat transport ( $F_q$ )	110.9 W m <sup>-2</sup>	244.2 W m <sup>-2</sup>
Mass flux ( $U_A$ )	$1.82 \times 10^4$ kg m <sup>-1</sup> s <sup>-1</sup>	$1.90 \times 10^4$ kg m <sup>-1</sup> s <sup>-1</sup>

increase, respectively, as  $T_{SE}$  increases until  $T_{SE} = 298$  K, at which point their slopes decrease markedly (Fig. 13b). In Fig. 13c, we see a maximum of  $u_B$  near  $T_{SE} = 297.5$  K and a minimum of  $u_E$  near 295.5 K. These seemingly disparate behaviors can be explained as follows.

The required variation of  $F_H$  as a function of  $T_{SE}$  is determined by the difference between the surface and TOA energy fluxes in the WP. For this study, we have assumed that the atmosphere alone must respond to changes in net fluxes across the atmosphere. As shown in Fig. 14b, the energy fluxes at the top and bottom of the atmosphere increase as  $T_{SE}$  increases. However, the energy flux at the surface increases at a much faster rate than that at the TOA. The lateral transport of moist static energy from the WP must therefore decrease, consistent with Fig. 13. The net energy flux at the surface of the CP region exceeds the net energy flux at the TOA of the CP region. As  $T_{SE}$  increases, so does the difference between energy fluxes at the surface and TOA (Fig. 14a). Because the CP imports less energy from the WP as  $T_{SE}$  increases, energy balance dictates that the CP must shrink as  $T_{SE}$  increases. These results provide a basis to explain the behaviors of the other quantities shown in Fig. 13.

As  $T_{SE}$  increases (for  $a_w$  fixed initially), the mean wind speed in the CPBL decreases and the surface evaporation rate in the CP decreases. Because we have assumed that the evaporation efficiency is fixed, a decreasing surface evaporation rate in the CP implies that less moisture is being supplied to the WP, and so  $F_q$  decreases. A weaker SST gradient causes  $u_B$  to decrease and thus contributes to a weaker evaporation rate in the WP. These two effects combine to decrease  $W_w$ .

In our model, the lapse rate and water vapor distribution in the CP free troposphere are controlled by the WP. Because  $W_w$  decreases, the CP free troposphere dries. Consequently, the radiative cooling rate in the CP free troposphere and, thus the subsidence rate, decrease slightly. By mass continuity, a weaker subsidence rate leads to slower easterlies. As a result, the Walker circulation slows, and  $F_H$  increases and  $F_q$  decreases (their magnitudes decrease).

The adjustment process described above balances the energy budget for the WP but not for the CP. As the

precipitable water and CP SST increase, the vertical energy flux divergence of the CP surpasses the lateral energy transport from the WP. Hence the fractional widths of the WP and CP must adjust in order to balance the CP energy budget. As the fractional width of the CP decreases, the magnitudes of  $F_q$  and  $F_H$  increase (because  $\sigma_w$  is in the denominator), and  $W_w$  must increase slightly in order to restore energy and moisture balance to the WP. However, the initial decrease of  $W_w$  due to the adjustment of the WP is larger than this slight increase.

Despite drying of the WP as  $T_{SE}$  increases, the mean wind speed in the layer of easterlies ( $u_L$ ) increases with  $T_{SE}$  for  $T_{SE} < 296$  K. This behavior is related to changes of the vertical velocity. Although the precipitable water decreases slightly in the CP free troposphere, the radiative cooling rate increases slightly as  $T_{SE}$  increases. Furthermore, the difference in dry static energy between the boundary layer and troposphere decreases as  $T_{SE}$  increases. Because we assume that the radiative cooling rate is balanced by subsidence heating, these two factors result in stronger subsidence. It can be shown that  $u_L$  is constrained by the width of the CP and the vertical velocity. Even though the width of the CP shrinks, the increase in vertical velocity dominates, and so  $u_L$  increases slightly for the range  $T_{SE} < 296$  K.

Beyond  $T_{SE} = 297$  K, the simulation becomes much more sensitive to increases of  $T_{SE}$ . The adjustment process is similar to that described above. As  $T_{SE}$  increases, the energy flux convergence of the CP increases rapidly (Fig. 14a), which requires  $a_w$  to increase rapidly. As before,  $W_w$  increases as  $a_w$  increases in order to balance the WP energy budget. In this regime,  $W_w$  increases much more rapidly.

In summary, the precipitable water in the WP must vary in order to accommodate the assumed moisture and energy balance of the system. As  $T_{SE}$  increases, the energy flux divergence in the CP increases. The fractional width of the CP must adjust to restore energy balance. As the fractional widths change, however, the energy and moisture budgets of the WP become unbalanced. Thus,  $W_w$  must vary in order to restore energy/moisture balance for the WP. For cases in which  $a_w$  increases moderately and  $u_B$  decreases with  $T_{SE}$ , the pre-

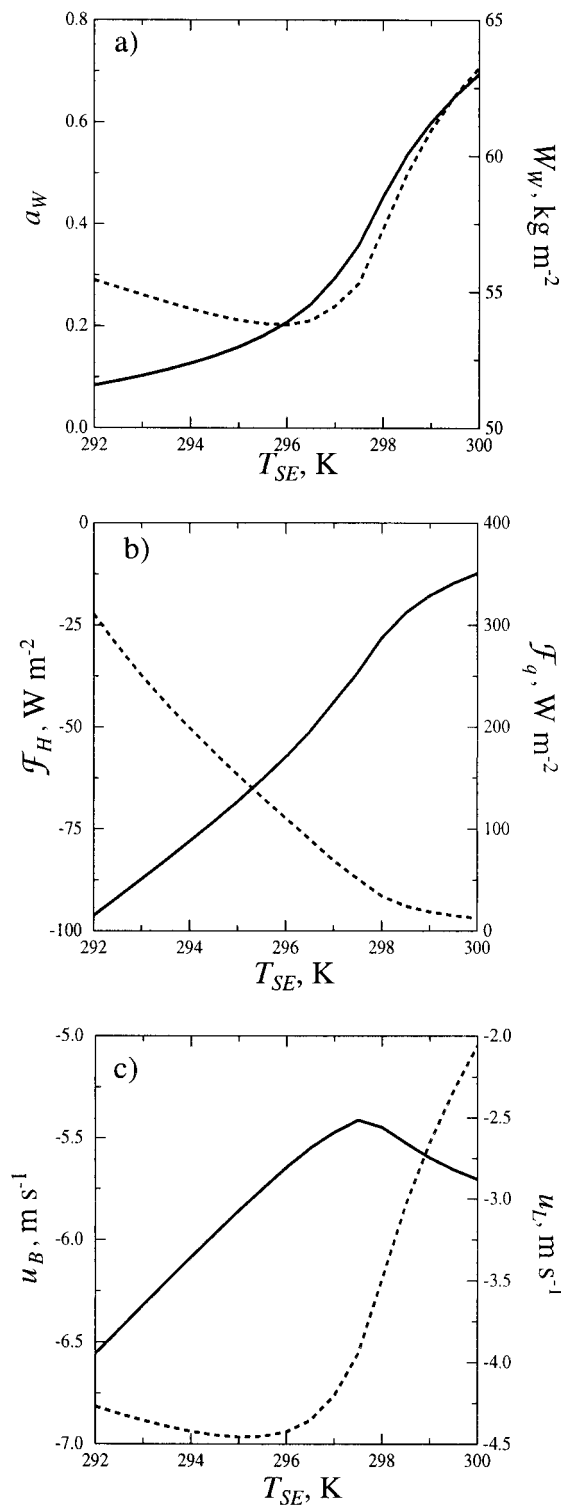


FIG. 13. Walker circulation as a function of CP SST for the atmosphere-only model. The WP SST was specified as 303 K. For each of these plots, the solid and dashed lines are associated with the left- and right-hand axes, respectively. (a) The fractional width of the WP and precipitable water in the WP region; (b) the lateral moist static energy and lateral latent heat transports between boxes; (c) the mean zonal winds in the boundary layer and in the layer of easterlies.

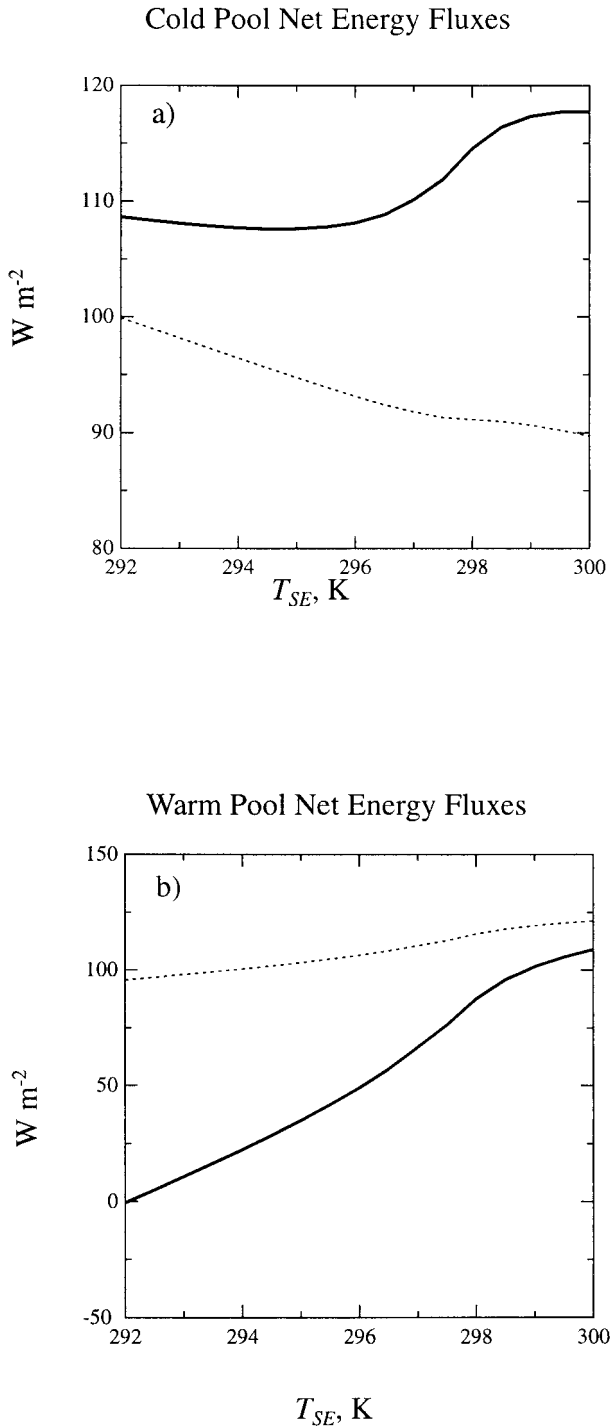


FIG. 14. Same as Fig. 13, except that energy fluxes for the surface (solid line) and TOA (dashed line) are plotted for (a) the CP and (b) the WP.

precipitable water decreases. For cases in which  $a_w$  increases strongly and  $u_B$  increases with  $T_{SE}$ ,  $W_w$  increases.

The maximum of  $u_B$  near  $T_{SE} = 297$  K is quite interesting. We prescribed the east-west SST difference for each case and the east-west pressure difference at

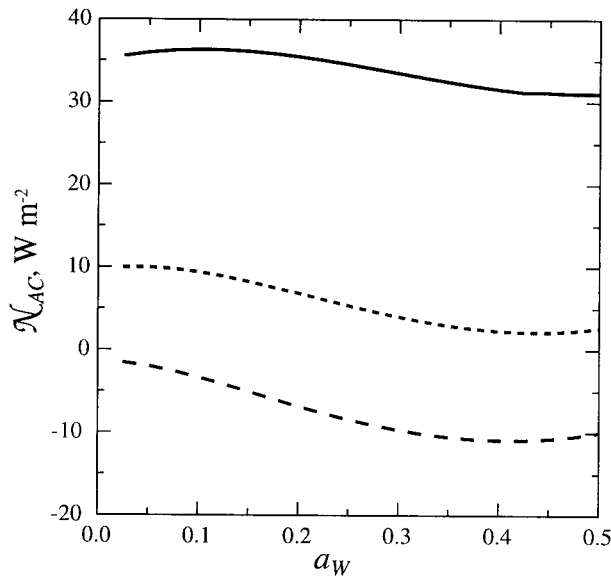


FIG. 15. The net energy imbalance of the CP,  $N_{AC}$ , plotted as a function of specified WP fractional width for IWP values of 0.05 (solid line), 0.10 (dotted line), and 0.15  $\text{kg m}^{-2}$  (dashed line).

the top of the TWI as 200 mb for all cases. As the fractional width of the CP decreases with  $T_{SE}$ , the pressure slope of the TWI increases. Even though the east-west SST difference decreases as  $T_{SE}$  increases, the magnitude of the SST gradient has a minimum at  $T_{SE} = 297$  K. Here we define the SST gradient as  $\partial T_s / \partial x = (T_{SE} - T_{SW}) / \sigma_C$  under the assumption that SST varies linearly in the CP. For  $T_{SE} > 297$  K, the magnitudes of the pressure gradient of the TWI and of the SST gradient increase as  $T_{SE}$  increases, and they therefore produce a maximum of  $u_B$ . As the CPBL wind speed increases, the surface latent heat flux in the CP increases slightly (rather than decreases strongly). This causes the net surface energy flux in the CP (solid curve in Fig. 14a) to flatten and leads to a flattening of the  $F_H$  and  $F_q$  curves (Fig. 13b). We conclude from this behavior that including a CPBL momentum budget in the model adds a much richer range of interactions (even if SSTs are fixed).

In order to illustrate the dependence of the solution on cloud radiative forcing, we have plotted in Fig. 15

the vertical energy flux divergence of the CP atmosphere, defined as  $N_{AC} = N_{\infty C} - N_{SC}$ , for three specified values of IWP as a function of  $a_w$ . According to [(B4) in appendix B], the specified IWP values of 0.05 (solid line), 0.10 (dotted line), and 0.15  $\text{kg m}^{-2}$  (dashed line) result in cloud fractions of 0.5, 0.67, and 0.75, respectively. For these runs, we specified  $T_{SW} = 303$  K and  $T_{SE} = 296$  K and searched for solutions. If a solution exists, then the curve crosses zero, that is,  $N_{AC} = 0$ , for a given IWP and  $a_w$ . As can be seen from the figure, no solution exists for the three specified values of IWP. For our base case, IWP = 0.12  $\text{kg m}^{-2}$  and  $f = 0.71$ , which produce net cloud radiative forcings of  $-7.5$  and  $-125$   $\text{W m}^{-2}$  at the top and bottom of the WP atmosphere, respectively. If we had plotted our base case with IWP = 0.12  $\text{kg m}^{-2}$ , the curve would have crossed zero for  $a_w = 0.207$ . This highlights the strong sensitivity of the solution to the cloud radiative forcing in the WP. Of course, we could have found solutions for the different values of specified IWP if we had allowed the SST to vary. Although the precipitable water can vary as a function  $a_w$ , the lateral energy transport from the WP cannot balance the vertical energy flux divergence of the CP unless the cloud radiative forcing rate is just so. Ramanathan and Collins (1991) proposed that high clouds over the WP affect the WP SST; our result seems to indicate that WP clouds exert a remote effect on the circulation.

Table 4 shows that the solution depends not only on the SST gradient, but also on the individual values of  $T_{SE}$  and  $T_{SW}$ . For the “warm case,” we specified  $T_{SW} = 305$  K and  $T_{SE} = 298$  K, consistent with the 7-K east-west SST difference in the base case. In response to higher SSTs across the Tropics, the CP energy flux divergence increased, but the vertical velocity just above the TWI decreased by 2.5  $\text{mb day}^{-1}$ . The model maintained energy balance in the CP by decreasing  $a_w$  and increasing  $W_w$ . The lapse rate in the Tropics (and in our model) closely follows the moist adiabat, which decreases as the SST increases. Hence the vertical velocity of the model decreases as SSTs in the Tropics increase. This response is identical to that noted by Betts and Ridgeway (1989), Miller (1997), LHK, and Clement and Seager (1999) under similar conditions.

For the cases presented in Figs. 13 and 14 the evap-

TABLE 4. Dependence on SST. The base case is for  $T_{SE} = 296$  K. The warm case is for  $T_{SE} = 298$  K.

Variable	Base case	Warm case
Specified $T_{SW}$	303 K	305 K
Fractional width of the WP ( $a_w$ )	0.207	0.064
$W_w$	53.8 $\text{kg m}^{-2}$	56.8 $\text{kg m}^{-2}$
$W_C$	18.1 $\text{kg m}^{-2}$	18.5 $\text{kg m}^{-2}$
Maximum vertical-mean zonal wind in the CPBL	$-5.6$ $\text{m s}^{-1}$	$-5.3$ $\text{m s}^{-1}$
Surface latent heat flux in CPBL	112.3 $\text{W m}^{-2}$	125.5 $\text{W m}^{-2}$
Lateral moist static energy transport ( $F_H$ )	$-57.4$ $\text{W m}^{-2}$	$-105$ $\text{W m}^{-2}$
Lateral latent heat transport ( $F_q$ )	111 $\text{W m}^{-2}$	461 $\text{W m}^{-2}$
Mass flux ( $U_A$ )	$1.82 \times 10^4$ $\text{kg m}^{-1} \text{s}^{-1}$	$1.70 \times 10^4$ $\text{kg m}^{-1} \text{s}^{-1}$

oration efficiency  $\Delta$  was specified as 1/2. The evaporation efficiency is defined as the fraction of evaporated water which is available for transport to the WP, that is, the fraction of water vapor that has not been precipitated out of the atmosphere. As the evaporation efficiency increases, a greater percentage of evaporated water vapor is transported to the WP. For  $T_{sw} = 303$  K and  $T_{se} = 296$  K, Fig. 16 shows how the model solution varies as a function of  $\Delta$ . As  $\Delta$  increases, more water vapor is advected to the WP, and so  $W_w$  must increase in order to maintain energy and moisture balance. This is precisely what we see in Fig. 16.

Recognizing that the amount of precipitable water over the CP may affect the intensity of the circulation, we designed an experiment to examine the effect of changing the outflow profile from convection. This experiment harkens back to the feedback mechanism proposed by Lindzen (1990) for a doubled  $\text{CO}_2$  climate. Lindzen hypothesized that, in response to a warming of the WP SST, cloud tops associated with convective activity would rise, and so dryer air would be advected into the subsiding regions of the Tropics. The subsidence would decrease in response to weaker radiative cooling of the dryer air. Although we do not allow SST to change in the current study, we can examine the response of the atmosphere to changing  $p_{\min}$  which is the minimum pressure level in the WP region from which air is advected to the CP region.

As discussed for the CP stand-alone results (Fig. 11), allowing the CP to receive water vapor from lower levels in the WP region causes the free troposphere over the CPBL to moisten. Table 5 illustrates the sensitivity of our model to the vertical distribution of WP moisture. Recall that we have assumed that the column water vapor over the central part of the CP free troposphere originates from the upper and midtroposphere of the WP region. For our base case,  $p_{\min}$  is assumed to be 500 mb. Suppose that the precipitable water originates from higher or lower in the WP free troposphere. For the “moist-outflow” and “dry-outflow” cases presented here, the  $p_{\min}$  levels used are 535 and 495 mb, respectively. As can be seen from Table 5, the solutions are quite different. As before,  $T_{sw}$  and  $T_{se}$  are specified, but the precipitable water and fractional widths are simulated.  $W_w$  in the dry-outflow case is a truly spectacular  $35.1 \text{ kg m}^{-2}$  larger than that simulated in the moist-outflow case. The CP free troposphere is also moister for the dry-outflow case. Although we tried to moisten the atmosphere in the moist-outflow case by allowing mass transport from warmer, moister, lower region of the WP, the atmosphere responded by drying. The converse is true for the dry-outflow case.

The dry-outflow and moist-outflow solutions differ because the radiative cooling rate increases as the precipitable water in the CP increases. When the specified value of  $p_{\min}$  is increased (i.e., outflow occurs at a lower altitude) for the moist-outflow case, air supplied to the CP is moister than air that emerges from higher altitudes

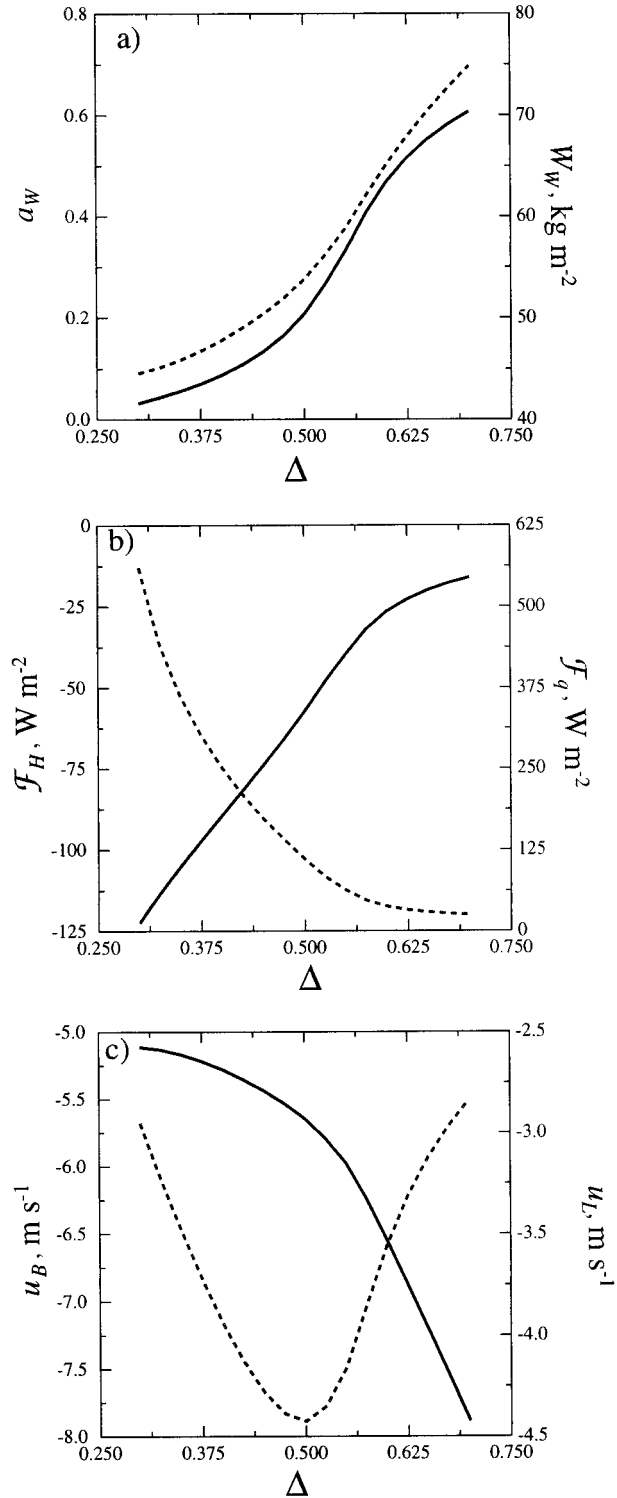


FIG. 16. Same as Fig. 13, except that the quantities are plotted as a function of the evaporation efficiency  $\Delta$ .

TABLE 5. Dependence on vertical distribution of moisture advection.

Variable	Moist outflow	Dry outflow
Fractional width of the WP ( $a_w$ )	0.094	0.644
$W_w$	49.5 kg m <sup>-2</sup>	84.6 kg m <sup>-2</sup>
$W_c$	17.0 kg m <sup>-2</sup>	26.5 kg m <sup>-2</sup>
Maximum vertical-mean zonal wind in the CPBL	-5.44 m s <sup>-1</sup>	-9.43 m s <sup>-1</sup>
Surface latent heat flux in CPBL	116 W m <sup>-2</sup>	105 W m <sup>-2</sup>
Lateral moist static energy transport ( $F_H$ )	-92.1 W m <sup>-2</sup>	-15.2 W m <sup>-2</sup>
Lateral latent heat transport ( $F_q$ )	289 W m <sup>-2</sup>	13.5 W m <sup>-2</sup>
Minimum advective level ( $p_{\min}$ )	535 mb	495 mb
Mass flux ( $U_A$ )	$1.93 \times 10^4$ kg m <sup>-1</sup> s <sup>-1</sup>	$8.60 \times 10^3$ kg m <sup>-1</sup> s <sup>-1</sup>

for the dry-outflow simulation. As a result, the radiative cooling rate intensifies and therefore produces a stronger subsidence rate, which causes the mass flux of the circulation to increase. Thus, lowering the outflow altitude causes the Walker circulation to intensify and the lateral energy transport from the WP to the CP to increase. By assumption, the Tropics must maintain energy balance, and so the CP region must expand ( $a_w$  must decrease) in order to reduce the net energy flux per unit area from the WP. Likewise, precipitable water in the WP must decrease in order to supply less energy to the CP. In nature, the SSTs could also change. The model therefore reaches equilibrium for lower values of  $W_w$  and  $a_w$ . This result demonstrates the sensitivity of our model to the amount and vertical distribution of water vapor over the CPBL.

Although these results indicate that the circulation is strongly influenced by the outflow level specified in the WP, our assumption of fixed SST makes it difficult to compare our results directly with Lindzen's hypothesis (1990). Our results do seem to indicate that the intensity of the circulation depend on the outflow level. It will be interesting to reevaluate these results in a follow-on study in which SSTs are allowed to vary. Rather than specifying the outflow level, it might also be worthwhile to parameterize the outflow level in terms of the SST gradient or some measure of the intensity of the circulation. A coupling between the SST gradient and the outflow level would allow us to study the interactions between the circulation and water vapor transport.

## 8. Summary and conclusions

We have described the formulation and coupling of models of the WP and CP regions. The surface wind speed for the WP region is calculated based on the mass flux from the CPBL. A simplified but physically based momentum budget is important for the CPBL. The parameterization for the free-tropospheric radiative cooling rate above the CPBL derives from the work of Stephens et al. (1994). The subsidence rate over the CPBL is computed, based on the observed balance between subsidence and radiative cooling. The hydrological cycle of the two-box model is fully interactive; the evaporation rate does not depend on a prescribed wind stress as in LHK, nor is it calculated as that which balances

the surface energy budget, as in Miller (1997). The effects of precipitation in the CPBL are prescribed. As described in KRS, the radiative effects of cirrus clouds over the WP are explicitly calculated, without assuming the cloud optical depth. In addition, the cloud fraction for the WP is calculated as described in section 3. The limitations are that SST has been prescribed, ocean heat transport has been ignored, and the slope of the boundary layer has been fixed.

Section 7 presents our results for the Walker circulation. For this study, we have neglected the radiative effects of clouds in the CP region. In our base case,  $T_{SW}$  was specified as 303 K, in accord with the observations. The most realistic simulation occurs for  $T_{SE} = 296$  K. In this case, the simulated values for  $W_w$  and  $W_c$  are 53.8 and 18.1 kg m<sup>-2</sup>, respectively, which compare favorably with a satellite-observed water vapor dataset presented in Fig. 12. The vertical-mean wind speed for the boundary layer is -5.6 m s<sup>-1</sup>, which compares well with observations presented by Battisti and Ovens (1995). The WP was found to be 0.207 of the total area. The simulated values for  $F_q$  and  $F_H$ , the lateral transports of latent heat and moist static energy, are 110.9 and -57.4 W m<sup>-2</sup>, respectively, which are quite close to the values prescribed in KRS.

We found that the solution depends strongly on the specified value of  $T_{SE}$ . As  $T_{SE}$  increases, the equilibrium values of  $a_w$  and  $W_w$  generally increases (although  $W_w$  actually decreases slightly for  $T_{SE} < 296$  K). This dependence results primarily from the adjustment of  $a_w$  in response to increasing vertical energy flux divergence in the CP as  $T_{SE}$  increased.

We also found that the solution is sensitive to the value of  $\Delta$ , which specifies the proportion of evaporated water vapor that is precipitated in the CPBL. For  $\Delta = 1$ , the precipitation rate in the CP region is zero, and all evaporated water vapor is transported laterally to the WP region. For  $\Delta = 0$ , the precipitation rate is 100%, and so none of the evaporated water vapor is transported to the WP region. In previous box models, the effects of precipitation in the CP region were not explicitly discussed. As shown in Fig. 16, the precipitable water and fractional width in the WP region increase strongly as  $\Delta$  increases. As the precipitation rate in the CP region decreases, the precipitable water of the WP increases.

Although the effect of precipitation rate in the CP region on precipitable water over the WP is somewhat obvious, our results give the first quantitative estimates of its influence.

Our “dry-outflow” and “moist-outflow” experiments demonstrate the crucial connection between water vapor amount and vertical distribution, and the tropical climate. As the water vapor increases over the CPBL, the radiative cooling rate and hence the mass flux of the Walker circulation increase. The moist-outflow solution therefore shows that if water vapor is advected to the CP region from a lower altitude in the WP region, the circulation speeds up. Because the circulation is faster, the fractional width and precipitable water of the WP region must decrease in order to balance the energy and moisture budgets. In fact, when we try to moisten the atmosphere for this experiment, the model adjusts so as to dry out.

We have presented results from a simplified toy model in order to show the sensitivity of the Walker circulation to the hydrological cycle in general and to the water vapor distribution in particular. Although our discussion has neglected the effects of stratocumulus clouds in the CP and of the ocean on the Walker circulation, their importance cannot be emphasized too strongly. As described by Kelly (1999), the Walker circulation is strongly modulated by ocean–atmosphere interactions and cloud–climate feedbacks. Rather than briefly discussing these ideas in our present study, we choose to consider these issues at length in our next paper. The key sensitivities of our model are to the individual SSTs in the WP and CP, to the east–west SST difference, to  $\Delta$ , to  $p_{\min}$ , and to  $t_{\text{prec}}$ . Equilibrium solutions with prescribed SSTs showed a strong sensitivity to  $\Delta$ , the evaporation efficiency. A future goal is to calculate  $\Delta$  in a simple way.

*Acknowledgments.* This project has been supported by the National Aeronautics and Space Administration under Grants NAG5-1058 and NAG8-981, and by the National Science Foundation under Grants ATM-8907414 and ATM-9100795, all to Colorado State University. ECMWF reanalysis data were obtained from NCAR. We thank two anonymous reviewers for their helpful comments and insightful suggestions.

## APPENDIX A

### Derivation of Moist Static Energy Budget for a Two-Box System

The steady-state vertically and horizontally integrated budget equation for moist static energy in the layer of easterlies is

$$h_L U_A + [\overline{h_{L+} M_L} - (\overline{N_L} - \overline{N_S})] \sigma_C = 0, \quad (\text{A1})$$

where  $h_L$  denotes the vertical-mean value of moist static energy in the layer of easterlies,  $h_{L+}$  is the moist static

energy just above  $p_L$ ,  $N_L$  is the net downward energy flux at  $p_L$ , and  $N_S$  is the net downward energy flux at the surface. In the definition of moist static energy given above,  $L$  is the latent heat of condensation,  $c_p$  is the heat capacity of air at constant pressure, and  $g$  is the acceleration due to gravity.

Because the lapse rate in the free troposphere is assumed to be horizontally uniform and controlled by the WP,  $h_{L+}$  depends only on  $p_L$ . From the steady-state budget for moist static energy for the upper troposphere,  $\overline{h_{L+} M_L} \sigma_C = U_A h_U - (\overline{N_T} - \overline{N_L}) \sigma_C$ , where  $N_T$  is the net energy flux at the tropopause and  $h_U$  is the vertical-mean moist static energy in the layer of westerlies. Substituting the right-hand side of this expression into (A1), the moist static energy budget reduces to the form written in Table 2. As described later, we compute the horizontal-mean vertical flux convergence of energy for the CP atmosphere (i.e., the right-hand side of the moist static energy budget). We use an approach that determines the longwave radiative cooling rate based on the emissivities and emission temperatures of the upper and lower layers of the troposphere.

## APPENDIX B

### Derivation of Diagnostic Equation for IWP

Following KRS, we assume that stratiform ice cloud is produced by convective detrainment, so that the rate of ice production is proportional to the convective precipitation rate  $P_C$ . Cloud ice removal is due to stratiform precipitation at rate  $P_S$  and to sublimation at rate  $S$ ; both  $P_S$  and  $S$  are parameterized in terms of vertically integrated cloud ice (IWP—ice water path). Neglecting horizontal advection of cloud ice, our prognostic equation is

$$\frac{d}{dt} \text{IWP} = \chi P_C - P_S - S, \quad (\text{B1})$$

where  $\chi$  is a nondimensional parameter. We assume that the stratiform precipitation rate satisfies

$$P_S = \begin{cases} 0, & \text{IWP} \leq c', \\ \frac{\text{IWP} - c'}{f t_{\text{prec}}}, & \text{IWP} > c', \end{cases} \quad (\text{B2})$$

where  $f$  is the fractional cloudiness above the WP and  $t_{\text{prec}}$  is an “autoconversion” timescale for the removal of ice by stratiform precipitation. As can be seen from (B2),  $c'$  represents a threshold of IWP below which no stratiform precipitation occurs. A threshold is reasonable because thin cirrus clouds rarely precipitate. In KRS,  $c'$  was implicitly assumed to be zero.

For simplicity, we assume that the sublimation rate is governed by

$$S = \text{IWP} / f t_s, \quad (\text{B3})$$

where  $t_s$  is a specified timescale for the sublimation of cloud ice. Note that  $f$  appears in the denominator of

(B3). As the fractional cloudiness decreases, more cloud edge for a given IWP becomes available so that the sublimation rate increases.

Given that upper-tropospheric anvil clouds are the only cloud type considered for the WP region, it seems reasonable to parameterize the fractional cloudiness in terms of the IWP. Rather than relying on a relatively complex parameterization as in Xu and Randall (1996), we assume for simplicity that the fractional cloudiness satisfies

$$f = \frac{\text{IWP}}{\text{IWP} + c}, \quad (\text{B4})$$

where  $c$  is a specified, dimensional parameter. As can be seen in (B4),  $f = 0$  for  $\text{IWP} = 0$  and  $f \rightarrow 1$  as the IWP becomes much larger than  $c$ .

Using and substituting (B2), (B3), and (B4) in (B1) we find that

$$\frac{d}{dt}\text{IWP} = \chi P - \frac{(1 + \chi)}{t_{\text{prec}}} \frac{(\text{IWP} - c')(\text{IWP} + c)}{\text{IWP}} - \frac{(\text{IWP} + c)}{t_s}. \quad (\text{B5})$$

If  $\text{IWP} < c'$ , then the second term on the right-hand side must vanish according to (B2); in that case, the cloud-ice time rate of change is determined by the first and third terms on the right-hand side. If the left-hand side of (B5) is neglected, then a quadratic equation for IWP results. The steady-state solution of (B5) reduces to (12) in the main body of the paper, if  $c = c'$  is assumed. The positive root has been chosen to ensure that the right-hand side of (12) is nonnegative. Our motivation for setting  $c = c'$  is to keep the model simple. In (B4), the value of  $c$  determines the amount of cloud ice required for  $f = 0.5$ . Because  $c'$  is the threshold for stratiform precipitation, the assumption that  $c = c'$  implies that no stratiform precipitation can occur unless  $f > 0.5$ . An additional practical reason for choosing  $c = c'$  is that, with this assumption, the right-hand side of (12) is guaranteed to be nonnegative.

#### REFERENCES

- Battisti, D. S., and D. D. Ovens, 1995: The dependence of the low-level equatorial jet on Hadley and Walker circulations. *J. Atmos. Sci.*, **52**, 3911–3931.
- Betts, A. K., and W. Ridgway, 1989: Climatic equilibrium of the atmospheric convective boundary layer over a tropical ocean. *J. Atmos. Sci.*, **46**, 2621–2641.
- Brown, R. G., and C. Zhang, 1997: Variability of midtropospheric moisture and its effect on cloud-top height distribution during TOGA COARE. *J. Atmos. Sci.*, **54**, 2760–2774.
- Charney, J. G., 1963: A note on large-scale motion in the tropics. *J. Atmos. Sci.*, **20**, 607–609.
- Clement, A., and R. Seager, 1999: Climate and the tropical oceans. *J. Climate*, **12**, 3383–3401.
- Deardorff, J. W., 1972: Parameterization of the planetary boundary layer for use in general circulation models. *Mon. Wea. Rev.*, **100**, 93–106.
- Geisler, J. E., 1981: A linear model of the Walker circulation. *J. Atmos. Sci.*, **38**, 1390–1400.
- Gill, A. E., 1980: Some simple solutions for heat-induced tropical circulation. *Quart. J. Roy. Meteor. Soc.*, **106**, 447–462.
- Hastenrath, S., 1998: Contribution to the circulation climatology of the eastern equatorial Pacific: Lower atmospheric jets. *J. Geophys. Res.*, **103** (D16), 19 433–19 451.
- Ingersoll, A. P., 1969: The runaway greenhouse: A history of water on Venus. *J. Atmos. Sci.*, **26**, 1191–1198.
- Kelly, M. A., 1999: A simple model of ocean–atmosphere interactions in the tropical climate system. Ph.D. dissertation, Colorado State University, 205 pp.
- , D. A. Randall, and G. L. Stephens, 1999: A simple radiative-convective model with a hydrological cycle and interactive clouds. *Quart. J. Roy. Meteor. Soc.*, **125A**, 837–869.
- Lacis, A., and J. E. Hansen, 1974: A parameterization for the absorption of solar radiation in the earth's atmosphere. *J. Atmos. Sci.*, **31**, 118–133.
- Larson, K., D. L. Hartmann, and S. A. Klein, 1999: The role of clouds, circulation, and boundary layer structure in the sensitivity of the tropical climate. *J. Climate*, **12**, 2359–2374.
- Lindzen, R. S., 1990: Some coolness concerning global warming. *Bull. Amer. Meteor. Soc.*, **71**, 288–299.
- , and S. Nigam, 1987: On the role of sea surface temperature gradients in forcing low-level winds and convergence in the tropics. *J. Atmos. Sci.*, **44**, 2418–2436.
- Miller, R. L., 1997: Tropical thermostats and low cloud cover. *J. Climate*, **10**, 409–440.
- Pierrehumbert, R. T., 1995: Thermostats, radiator fins, and the runaway greenhouse. *J. Atmos. Sci.*, **52**, 1784–1806.
- Ramanathan, V., and W. Collins, 1991: Thermodynamic regulation of ocean warming by cirrus clouds deduced from observations of the 1987 El Niño. *Nature*, **351**, 27–32.
- Rodgers, C. D., 1967: The use of emissivity in atmospheric radiation calculations. *Quart. J. Roy. Meteor. Soc.*, **93**, 43–54.
- Rosenlof, K. H., D. E. Stevens, J. R. Anderson, and P. E. Ciesielski, 1986: The Walker circulation with observed zonal winds, a mean Hadley cell, and cumulus friction. *J. Atmos. Sci.*, **43**, 449–467.
- Salathé, E. P., Jr., and D. L. Hartmann, 1997: A trajectory analysis of tropical upper-tropospheric moisture and convection. *J. Climate*, **10**, 2533–2547.
- Sherwood, S. C., 1999: Feedbacks in a simple prognostic tropical climate model. *J. Atmos. Sci.*, **56**, 2178–2200.
- Stephens, G. L., and P. J. Webster, 1979: Sensitivity of radiative forcing to variable cloud and moisture. *J. Atmos. Sci.*, **36**, 1542–1556.
- , and T. J. Greenwald, 1991: The Earth's radiation budget and its relation to atmospheric hydrology. 1. Observations of the clear sky greenhouse effect. *J. Geophys. Res.*, **96**, 15 311–15 324.
- , A. Slingo, M. J. Webb, P. J. Minnett, P. H. Daum, L. Kleinman, I. Wittmeyer, and D. A. Randall, 1994: Observations of the Earth's energy budget in relation to atmospheric hydrology. Part IV: Atmospheric column radiative cooling over the world's oceans. *J. Geophys. Res.*, **99**, 18 585–18 604.
- Sun, D.-Z., and Z. Liu, 1996: Dynamic ocean–atmosphere coupling: A thermostat for the tropics. *Science*, **272**, 1148–1150.
- Xu, K.-M., and D. A. Randall, 1996: A semiempirical cloudiness parameterization for use in climate models. *J. Atmos. Sci.*, **53**, 3084–3102.